Supplementary Information

Dynamic lanthanides exchange between quadruple-stranded cages: the effect of ionic radius differences on kinetics and thermodynamics

Marzio Rancan,*[a] Maria Rando,[b] Luigi Bosi,[b] Alice Carlotto,[b] Roberta Seraglia,[c] Jacopo Tessarolo,[d] Silvia Carlotto,[a,b] Guido H. Clever[d] and Lidia Armelao[b,e]

[a]Institute of Condensed Matter Chemistry and Technologies for Energy (ICMATE), National Research Council (CNR), c/o Department of Chemical Sciences, University of Padova, via F. Marzolo 1, 35131 Padova, Italy.

[b]Department of Chemical Sciences, University of Padova, via F. Marzolo 1, 35131 Padova, Italy.

[c]Institute of Condensed Matter and Technologies for Energy (ICMATE), National Research Council (CNR), Corso Stati Uniti, 4, 35127 Padova, Italy.

[d]Department of Chemistry and Chemical Biology, TU Dortmund University, 44227 Dortmund, Germany.

[e]Department of Chemical Sciences and Materials Technologies (DSCTM), National Research Council (CNR), Piazzale A. Moro 7, 00185 Roma, Italy.

* marzio.rancan@cnr.it and marzio.rancan@unipd.it

Index

1. Syntheses

Reagents were purchased from Aldrich and used as received. The elemental analyses were carried out with a Flash 2000 Thermo Scientific Analyzer at the Department of Chemical Sciences of the University of Padova.

1.1 Synthesis of preL

p-bromoacetophenone (3.58 g, 18.0 mmol), tert-butylcarbammate (0.70 g, 6.0 mmol), K_3PO_4 (7.64 g, 36.0 mmol), and CuI (0.35 g, 1.8 mmol), have been added in a Schlenk tube under argon atmosphere. Anhydrous toluene has been added as solvent (30 ml), together with N,N-dimethylethylenediamine (0.6 ml, 5.6 mmol). The mixture has been reacted at 110 °C for 45 h, under vigorous stirring. The reaction has been quenched by the addition of water (100 ml) and ethyl acetate (180 ml). The organic phase has been washed with water (3x100 ml), dried over $MgSO_4$ and the solvent has been removed under reduced pressure resulting in 3.44 g of a dark orange dense oil. The product has been purified by SiO_2 column chromatography (n-hexane/ethyl acetate 6:4) to give 2.06 g of a yellow solid. Yield: 97%

Elemental analysis for **preL** ($C_{21}H_{23}NO_4$): calculated C 71.37%, H 6.56%, N 3.96%; found C 71.25%, H 6.64%, N 4.03%.

^{1}H-NMR ($CDCl_3$, 200 MHz, T = 25 °C) δ[ppm] = 7.92 (4H, AA' in AA'BB' m, $H_{2,2'}$), 7.26 (4H, BB' in AA'BB' m, $H_{3,3'}$), 2.59 (6H, s, H_1), 1.47 (9H, s, H_4).

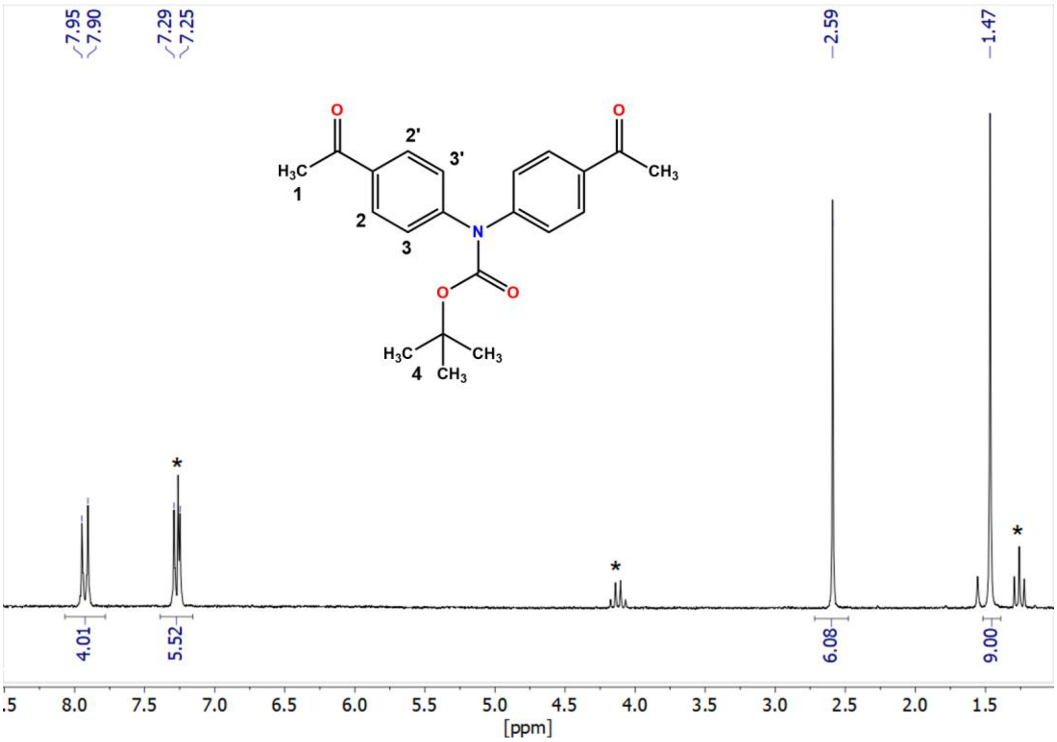

Figure S1 ^{1}H-NMR (25 °C, 200 MHz) spectrum of **preL** in $CDCl_3$. Solvent signals are marked with an asterisk.

1.2 Synthesis of L

Metallic Na (0.67 g, 29.1 mmol) has been dissolved in absolute ethanol (40 ml), in a 100 ml 3 necks round bottom flask, under argon atmosphere. After the solution reached room temperature, ethyl trifluoroacetate (5.0 ml, 42.0 mmol) and **preL** (2.06 g, 5.8 mmol) have been added, under vigorous stirring. In order to solubilize **preL**, the mixture has been heated to 65 °C. After that, the reaction mixture has been stirred at room temperature overnight. The solvent has been removed under reduced pressure. After addition of water (100 ml) and HCl 10% aqueous solution (10 ml), the formation of a yellow precipitate occurred. The solution has been extracted with CH_2Cl_2 (3x60 ml). The organic phase has been dried over $MgSO_4$ and the solvent has been removed under reduced pressure and the resulting yellow powder has been purified by recrystallization from ethyl acetate/*n*-hexane (1:2). The final product is obtained as yellow microcrystals (2.20 g). Yield: 70%. Compound purity has been confirmed by NMR and elemental analysis.

Elemental analysis for **L** ($C_{25}H_{21}F_6NO_6$): calculated C 55.05%, H 3.88%, N 2.57%; found C 54.92%, H 3.96%, N 2.63%.

^{1}H-NMR (400MHz, $CDCl_3$, T = 25°C): δ [ppm] = 15.13 (2H, s, H_2), 7.93 (4H, AA' part of an AA'BB' m, $H_{3,3'}$), 7.32 (4H, BB' part of an AA'BB' m, $H_{4,4'}$), 6.54 (2H, s, H_1), 1.48 (9H, s, H_5).

^{13}C-NMR (400MHz, $CDCl_3$, T = 25°C): δ [ppm] = 184.86 (s, C_4), 177.27 (q, C_2, $^2J_{C\text{-}F}$ = 36.7 Hz), 152.44 (s, C_9), 147.31 (s, C_8), 130.13 (s, C_5), 128.49 (s, C_6), 126.91 (s, C_7), 116.88 (q, C_1, $^1J_{C\text{-}F}$ = 281.5 Hz), 92.22 (q, C_3, $^3J_{C\text{-}F}$ = 2.0 Hz), 83.16 (s, C_{10}), 28.07 (s, C_{11}).

^{1}H-NMR (DMF-d_7, 300 MHz, T = 25 °C) δ[ppm] = 8.28 (4H, AA' in AA'BB' m, $H_{2,2'}$), 7.53 (4H, BB' in AA'BB' m, $H_{3,3'}$), 7.12 (2H, s, H_1), 1.48 (9H, s, H_4). OH signal not visible in DMF-d_7.

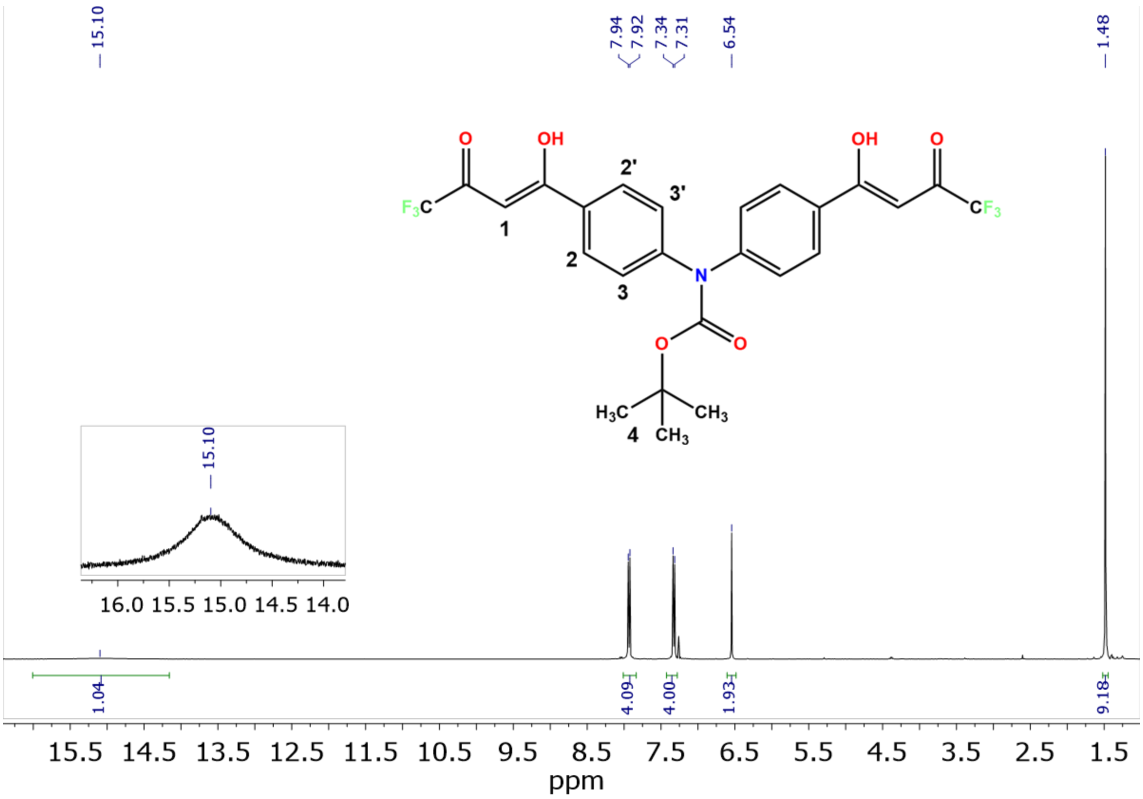

Figure S2 ^{1}H-NMR (25 °C, 400MHz) spectrum of **L** in $CDCl_3$.

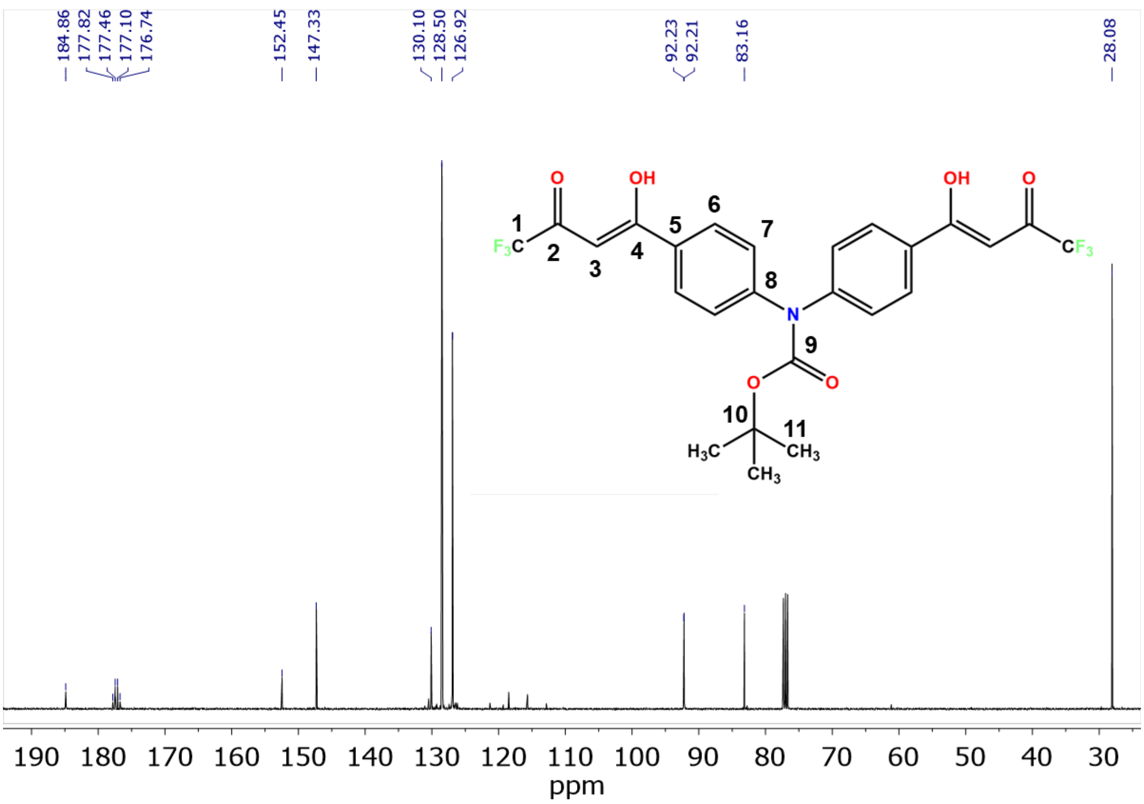

Figure S3 ^{13}C-NMR (25 °C, 400MHz) spectrum of **L** in $CDCl_3$.

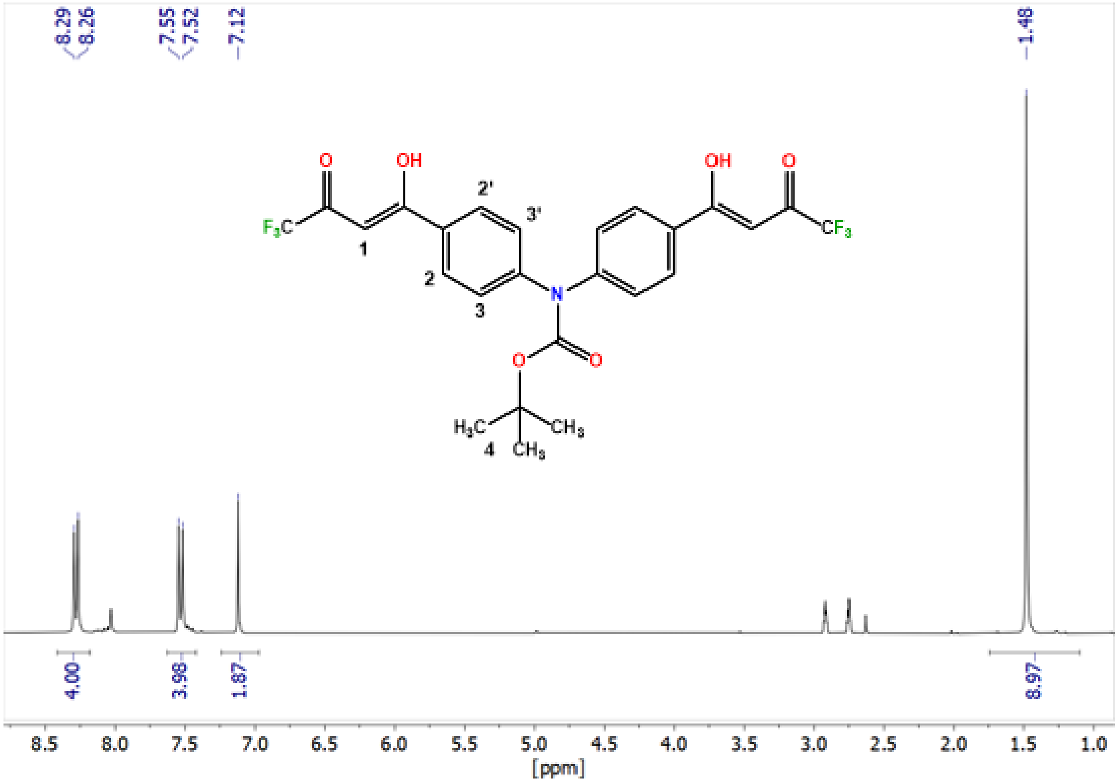

Figure S4 ^{1}H-NMR (25 °C, 300MHz) spectrum of **L** in DMF-d$_7$.

1.3 Syntheses of {[Ln_2L_4]$(X)_2$} cages

Ln = La, Nd, Eu, Tb, Er, Tm, Lu; cation X = NEt_4^+, DCHA$^+$

For all the syntheses the ratio Ln^{3+}:ligand:base used is equal to 1:2.5:5. All the {[Ln_2L_4]$(X)_2$} cages have been obtained with the following general procedure. The ligand (0.05 mmol) and the base (0.1 mmol) have been dissolved in 5 ml of ethanol. To this solution, a solution of the lanthanide salt (0.020 mmol) in 2 ml of ethanol, has been added dropwise. The formation of a white precipitate occurred. The mixture has been left under vigorous stirring for 3 hours, then filtered and the obtained powder has been washed with cold ethanol to give the pure product.

The cages have been prepared employing different bases and hence counter cations (tetraethylammonium hydroxide NEt_4OH, dicyclohexylamine DCHA), see Table S1.

Table S1 Reagents and yields for the syntheses of $\{[Ln_2L_4](X)_2\}$ cages. X = NEt_4^+, $DCHA^+$.

cage	Ln salt	base	yield [%]
$\{[La_2L_4](NEt_4)_2\}$	$La(NO_3)_3 \cdot 6H_2O$	NEt_4OH (25%, MeOH)	57
$\{[La_2L_4](DCHA)_2\}$	$La(NO_3)_3 \cdot 6H_2O$	DCHA	57
$\{[Nd_2L_4](NEt_4)_2\}$	$Nd(NO_3)_3 \cdot 6H_2O$	NEt_4OH (25%, MeOH)	34
$\{[Nd_2L_4](DCHA)_2\}$	$Nd(NO_3)_3 \cdot 6H_2O$	DCHA	34
$\{[Eu_2L_4](NEt_4)_2\}$	$EuCl_3 \cdot 6H_2O$	NEt_4OH (25%, MeOH)	78
$\{[Eu_2L_4](DCHA)_2\}$	$EuCl_3 \cdot 6H_2O$	DCHA	78
$\{[Tb_2L_4](NEt_4)_2\}$	$TbCl_3 \cdot 6H_2O$	NEt_4OH (25%, MeOH)	79
$\{[Tb_2L_4](DCHA)_2\}$	$TbCl_3 \cdot 6H_2O$	DCHA	79
$\{[Er_2L_4](NEt_4)_2\}$	$Er(CF_3SO_3)_3$	NEt_4OH (25%, MeOH)	16
$\{[Er_2L_4](DCHA)_2\}$	$Er(CF_3SO_3)_3$	DCHA	16
$\{[Tm_2L_4](NEt_4)_2\}$	$Tm(NO_3)_3 \cdot 5H_2O$	NEt_4OH (25%, MeOH)	43
$\{[Tm_2L_4](DCHA)_2\}$	$Tm(NO_3)_3 \cdot 5H_2O$	DCHA	43
$\{[Lu_2L_4](NEt_4)_2\}$	$Lu(NO_3)_3 \cdot xH_2O$	NEt_4OH (25%, MeOH)	56
$\{[Lu_2L_4](DCHA)_2\}$	$Lu(NO_3)_3 \cdot xH_2O$	DCHA	56

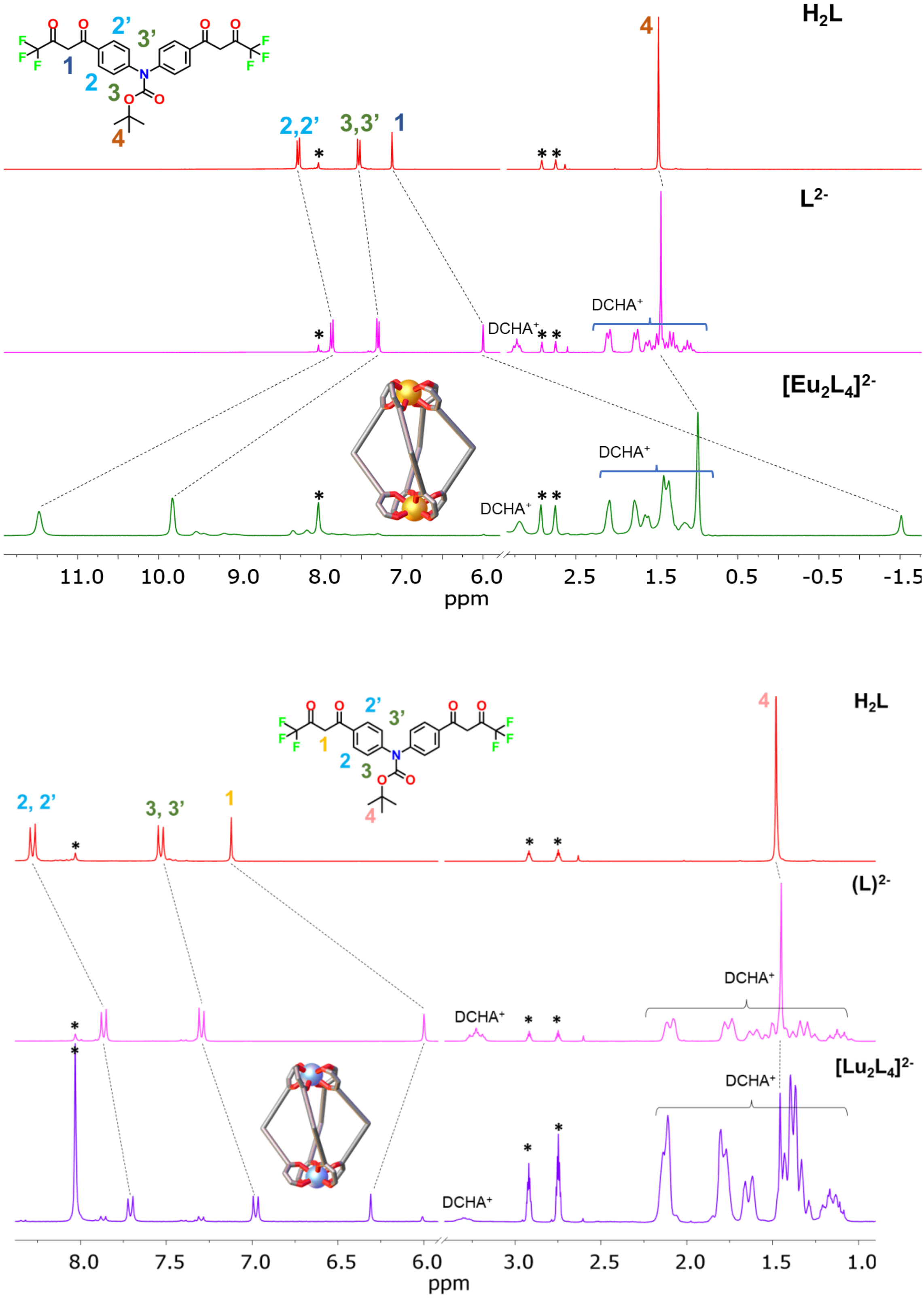

Figure S5 [1]H-NMR spectra (25 °C, 300 MHz, DMF-d7) of ligand H_2L, deprotonated ligand L^{2-}, cage $[Eu_2L_4]^{2-}$ and cage $[Lu_2L_4]^{2-}$. *=DMF.

2. Single crystal X-ray diffraction

Single crystals for the Eu cage were obtained from mother liquors (ethanol) slow evaporation. Ligand single crystal were obtained by slow evaporation of an acetonitrile/cyclo-hexane solution.

Data for ligand **L** were collected using an Oxford Diffraction Gemini E diffractometer, equipped with a 2K × 2K EOS CCD area detector and sealed–tube Enhance (Mo) and (Cu) X–ray sources. A suitable single crystal of **L** was fastened on a nylon loop and measured at room temperature. Detector distance has been set at 45 mm. The diffraction intensities have been corrected for Lorentz/polarization effects as well as with respect to absorption. Empirical multi-scan absorption corrections using equivalent reflections have been performed with the scaling algorithm SCALE3 ABSPACK. Data reduction, finalization and cell refinement were carried out through the CrysAlisPro software. Accurate unit cell parameters were obtained by least squares refinement of the angular settings of strongest reflections, chosen from the whole experiment.

A suitable crystal for the Eu cage was mounted at room temperature in NVH oil and measured at 100K. Data were collected on a Bruker D8 Venture diffractometer equipped with an INCOATEC micro focus sealed tube (Iμs 3.0), using using MoKα radiation on a four axis κ-goniometer, equipped with an Oxford Cryostream 800 and a Photon 100 detector. Data integration was done with SAINT, data scaling and absorption correction were performed with SADABS, in the APEX3 software.

The structures were solved with Olex2[1] by using ShelXT[2] structure solution program by Intrinsic Phasing and refined with the ShelXL[3] refinement package using least-squares minimization. In the last cycles of refinement, non-hydrogen atoms were refined anisotropically. Hydrogen atoms were included in calculated positions, and a riding model was used for their refinement. Details for each structure refinement are below reported along with crystallographic table (Table S2) and asymmetric unit images.
Cambridge Crystallographic Data Centre (CCDC) numbers 2150922 and 2150923 contain the supplementary crystallographic data for this paper. These data are provided free of charge by the joint CCDC and Fachinformationszentrum Karlsruhe Access Structures service www.ccdc.ca-m.ac.uk/structures.

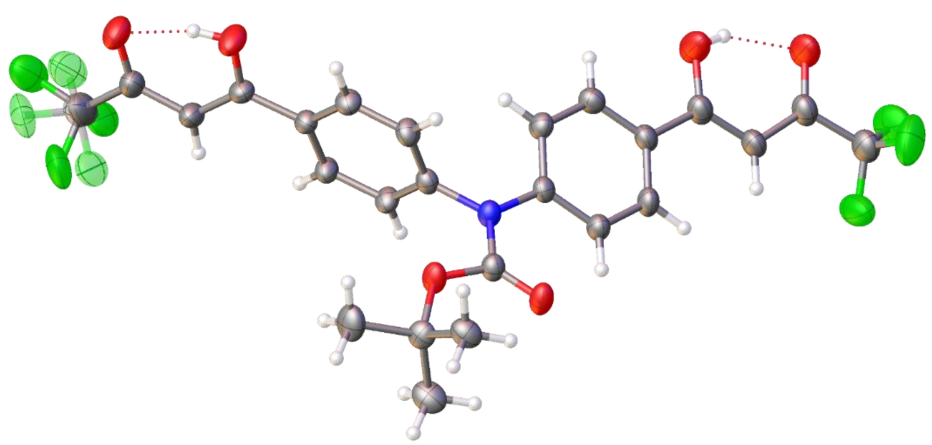

Figure S6 Asymmetric unit of **L**, thermal ellipsoid drawn at 30% probability level. Color code: C, grey; O, red; N, blue; F, green; H, white. Disordered parts translucent.

2.1 Refinement details for L

Ligand **L** crystallizes as very thin needles (0.01 × 0.01 × 0.1-0.2 mm) with not significative diffractions below 0.9 Å. A terminal CF_3 group have been split in two parts the occupancies of which were constrained to sum to 1.0. To better model these disordered groups, SADI restrains for C-F and F···F distances were applied and EADP constrains were applied to selected F atoms. RIGU restrains were applied. Reflections with error/esd > 10 have been omitted.

2.2 Refinement details for Eu cage

The compound crystallizes in the P-1 space group. In the asymmetric unit, two independent helicates are present as enantiomer pair, the *P* and *M* form (Figures S7a and S8), hence, the unit cell contains four helicates (two *M* and two *P*), Figures S7b. Some terminal CF_3 groups, a tert-butyl group and the ethyl chains of the NEt_4^+ cations hosted by the cages have been split in two parts the occupancies of which were constrained to sum to 1.0. To better model these disordered groups, SADI restrains for C-F, C-C, C-N and F···F distances were applied and EADP constrains were applied to selected atoms. RIGU restrains were applied to C, N, O and F atoms. The final Fourier map revealed the presence of non-negligible residual peaks located in a large array of voids and channels as illustrated in Figure S9. A total accessible void volume per unit cell of 1576.5 Å^3 was calculated (mask routine of OLEX2, probe radius 1.2 Å) corresponding to the 11.5% of the total unit cell volume. These voids are highly solvated with disordered solvent, a count of 369 electrons per unit cell were found. This value closely fits the presence of 12 ethanol and 4 water molecules which account for 370 electrons. In the final refinement cycles, EXTI command was applied.

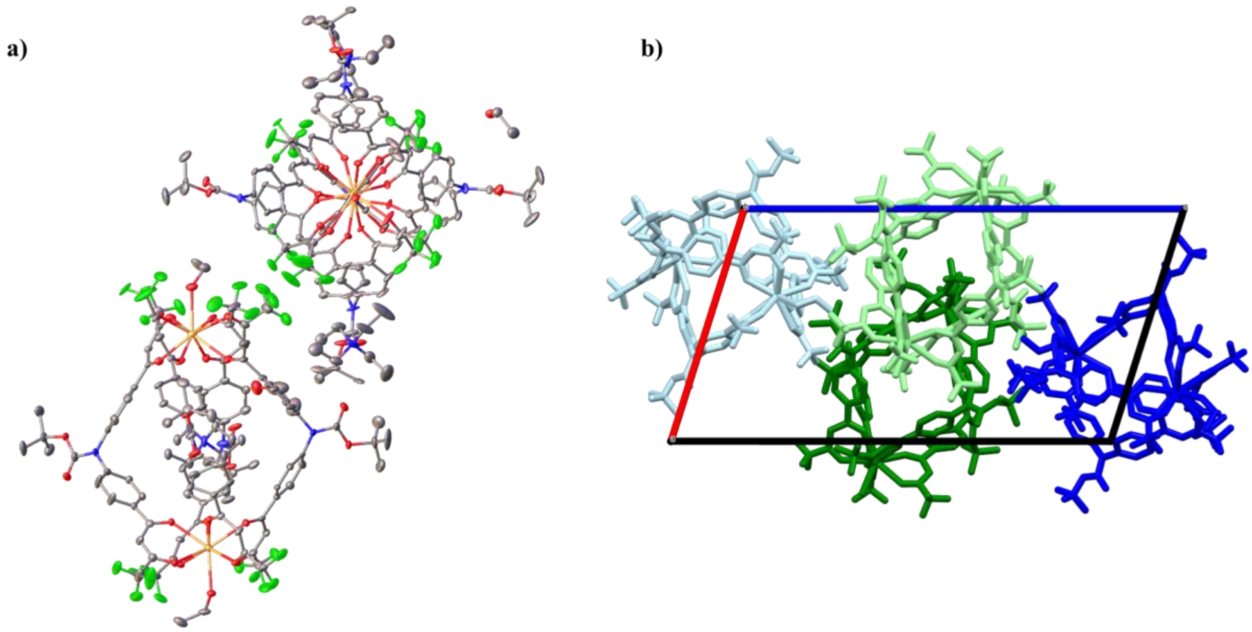

Figure S7 a) Asymmetric unit with thermal ellipsoid drawn at 50% probability level. Color code: C, grey; O, red; N, blue; F, green; Eu, orange. H atoms and disordered parts omitted for clarity. b) Unit cell content (view along *b* axis): dark and light blue ethanol-coordinated *M* and *P* helicates, respectively; dark and light green water-coordinated *P* and *M* helicates, respectively.

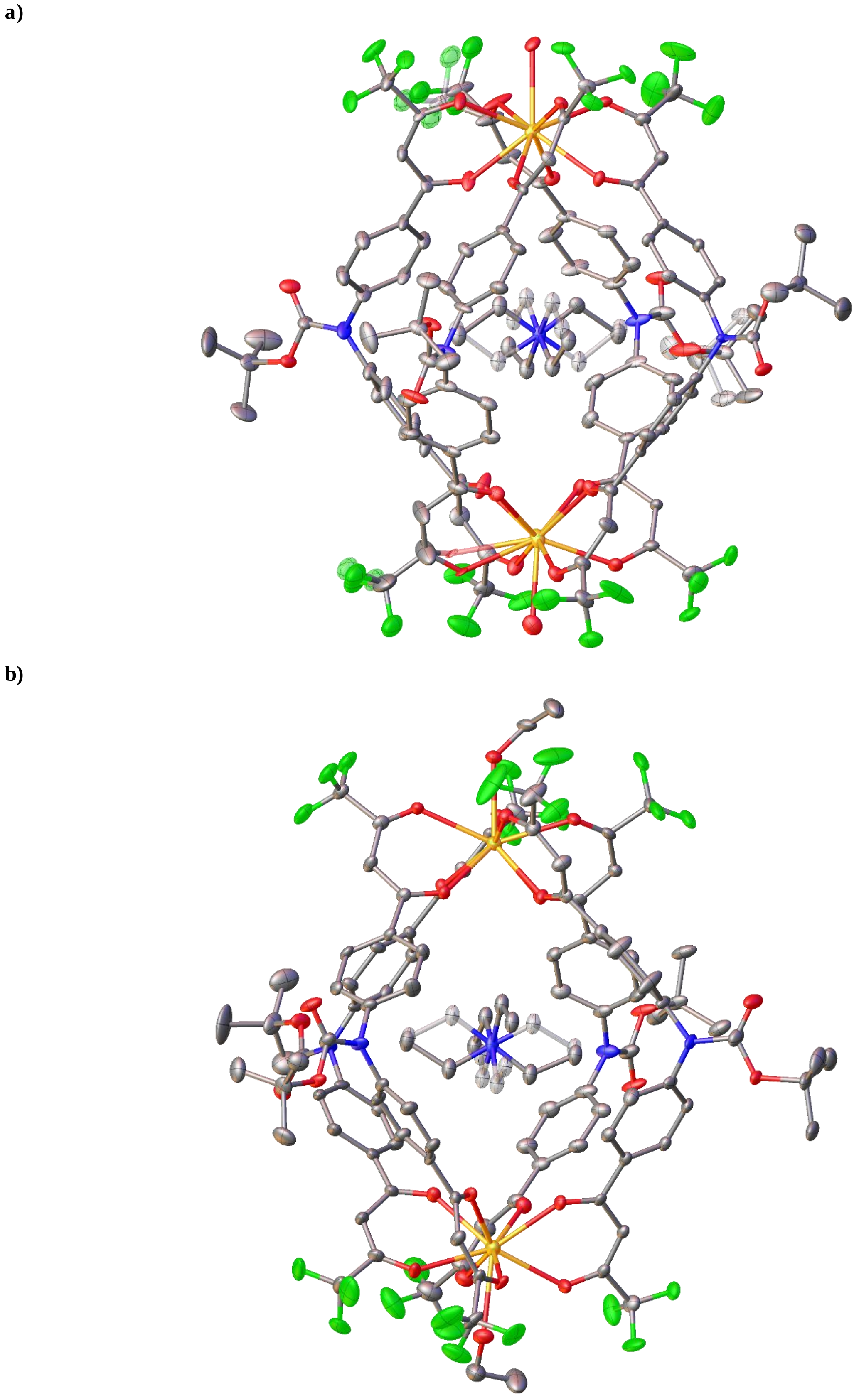

Figure S8 a) Helicate *P* and b) helicate *M* in the asymmetric unit. Thermal ellipsoid drawn at 50% probability level. Color code: C, grey; O, red; N, blue; F, green; Eu, orange. Disordered parts translucent. H atoms, external NEt_4^+ cations and solvent molecules omitted for clarity.

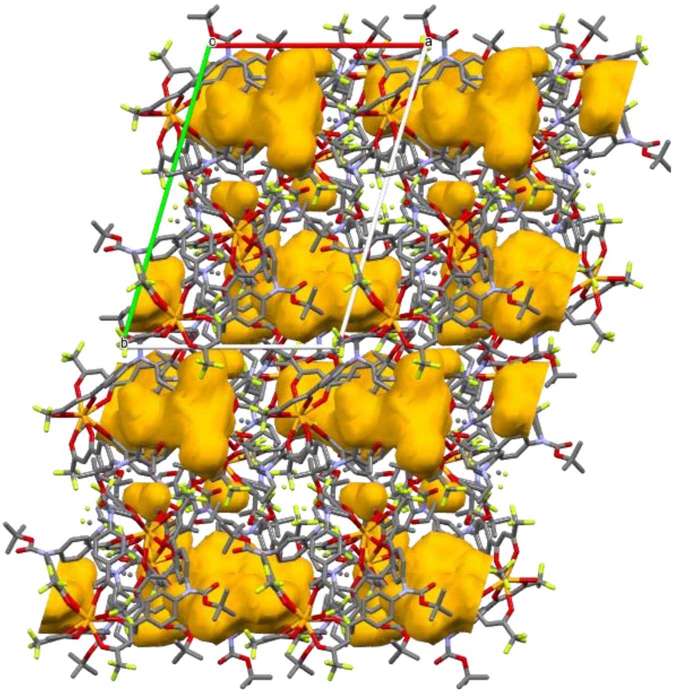

Figure S9 Voids (yellow) in the crystal packing (*ab* plane).

Table S2 Crystal data and structure refinement.

	L	**Eu cage**
Empirical formula	$C_{25}H_{21}F_6NO_6$	$C_{240}H_{259}Eu_4F_{48}N_{12}O_{54}$
Formula weight/ g mol^{-1}	545.43	5695.42
Temperature/K	296.0(3)	100.0
Crystal system	monoclinic	triclinic
Space group	$P2_1/n$	P-1
a/Å	19.326(3)	18.0830(10)
b/Å	5.6604(10)	25.6567(16)
c/Å	24.603(4)	32.1270(19)
α/°	90	98.535(2)
β/°	112.609(19)	104.813(2)
γ/°	90	103.262(2)
Volume/Å^3	2484.6(8)	13681.9(14)
Z	4	2
ρ_{calc} / g cm^3	1.458	1.382
μ/mm^{-1}	1.167	1.008
F(000)	1120.0	5798.0
Crystal size/mm^3	0.11 × 0.01 × 0.01	0.09 × 0.03 × 0.01
Radiation	Cu Kα (λ = 1.54184)	MoKα (λ = 0.71073)
2Θ range for data collection/°	7.384 to 117.842	3.964 to 52.744
Index ranges	$-21 \leq h \leq 15, -6 \leq k \leq 4, -20 \leq l \leq 27$	$-22 \leq h \leq 22, -32 \leq k \leq 32, -40 \leq l \leq 40$
Reflections collected	8649	831115
Independent reflections	3496 [R_{int} = 0.0603, R_{sigma} = 0.0965]	55848 [R_{int} = 0.1681, R_{sigma} = 0.0624]
Data/restraints/parameters	3496/343/361	55848/1430/3265
Goodness-of-fit on F^2	0.944	1.041
Final R indexes [I>=2σ (I)]	R_1 = 0.0930, wR_2 = 0.1935	R_1 = 0.0776, wR_2 = 0.1822
Final R indexes [all data]	R_1 = 0.1707, wR_2 = 0.2194	R_1 = 0.1003, wR_2 = 0.1952
Largest diff. peak/hole / e Å^{-3}	0.31/-0.22	3.35/-3.43
CCDC number	2150922	2150923

3. Computational details

The Amsterdam Density Functional (ADF) program (version 2013.01) was employed for calculations.[4] The generalized gradient approximation (GGA) PBE exchange-correlation functional[5] was used, combined with the TZ2P basis set. The TZ2P is a Slater-type triple-ζ quality basis sets augmented with two sets of polarization functions for all the atoms. Moreover, the small frozen-core approximation was employed for core shell electrons. Core shells up to level 4d for La and 1s for O, C, N and F were kept frozen. Scalar relativistic effects were considered using the scalar zeroth-order regular approximation (ZORA).[6–8] The numerical integration grid is a refined version of the fuzzy-cells integration scheme developed by Becke. Solvent effects were also considered using the COnductor-like Screening MOdel (COSMO)[9] with the default parameters for acetonitrile (dielectric constant $\varepsilon = 37.5$ and a solvent-excluding surface radius of 2.76 Å), while dispersion corrections are included as implemented by Grimme (Grimme3 BJDAMP).[10] Solvent effects and dispersion correction are included during the optimization calculation.

The binding energy (BE) between the solvent molecules and the cage have been obtained according equation S1:

$$BE = [E_{9cage2S} - (2E_S + E_{8cage})]/2 \qquad \text{eq. S1}$$

where $E_{9cage2S}$ is the energy of the cage-solvent system (nona-coordinated cage), E_S and E_{8cage} are the energies of the isolated solvent molecule and of the octa-coordinated cage, respectively.

a) **b)**

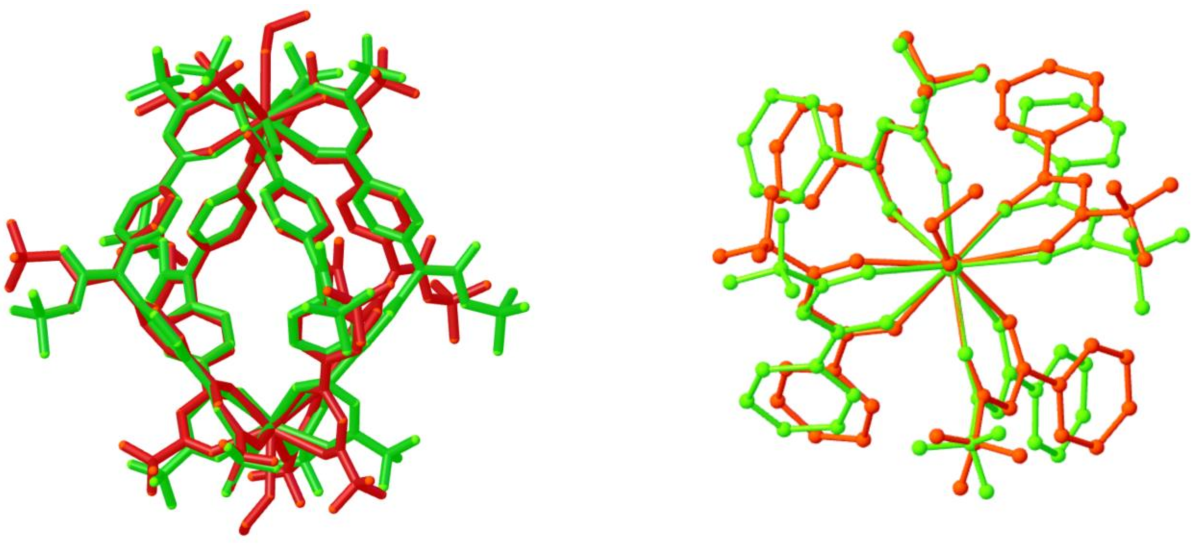

Figure S10 a) Overlay of the nona-coordinated XRD Eu cage structure (orange, *M* helicate) and the octa-coordinated DFT-optimised La cage (green, *M* helicate), side view, H atoms and NEt_4^+ guests omitted for clarity. b) Magnification of the coordination environment of the Ln ions (top view, only half cage is shown, H atoms omitted for clarity).

Table S3 Energies and structures of the DFT-optimized cages. Color code: C, grey; O, red; N, blue; F, green; La, dark blue; H, white.

	Optimized structure	Energy (kcal/mol)
Nona-coordinated cage with EtOH *M* helicate	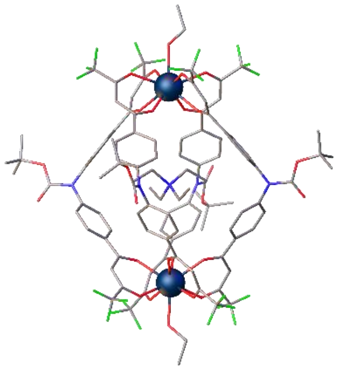	-40681.12
Octa-coordinated cage *M* helicate	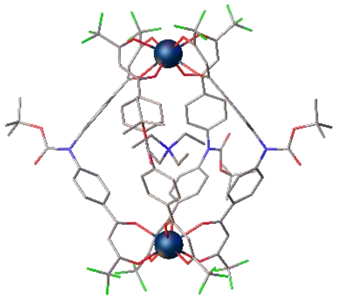	-38489.81
Nona-coordinated cage with H_2O *P* helicate	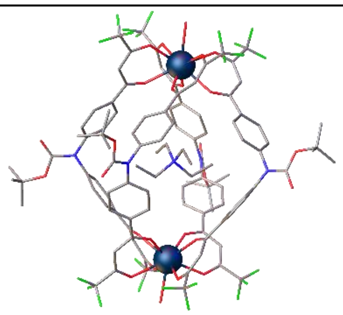	-39172.86
Octa-coordinated cage *P* helicate	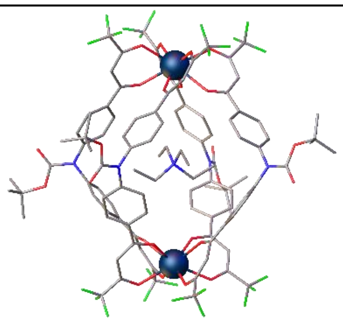	-38488.74
Isolated water molecule	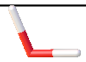	-334.62
Isolated ethanol molecule	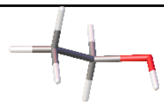	-1087.13

4. ESI-MS measurements

Electrospray mass spectrometric measurements (ESI-MS) were performed using a LCQ Fleet ion trap instrument (ThermoFisher), equipped with a HESI source, operating in negative ion mode. The mass spectra were acquired using the following experimental parameters: T_{HESI} = 35 °C; $T_{transfer\ capillary}$= 275 °C; Voltage HESI= 4 kV; nebulizer gas flow rate (N_2): 10 a.u.; auxiliary gas flow rate (N_2): 5 a.u. Sample {$[Ln_2L^X_4](cat)_2$} solutions (10^{-6} M in acetonitrile) was introduced by direct infusion using a syringe pump at a flow rate of 8 $\mu l \cdot min^{-1}$.

5. ESI-MS quantitative analysis: reproducibility and cages concentrations

In order to apply ESI-MS to monitor the concentration of the different species at different times, we hypothesized that the $[Ln_2L_4]^{2-}$ species should have comparable ionization efficiencies. To confirm this hypothesis, the ESI-MS spectrum of a solution containing equimolar amounts of the two homometallic cages $[Ln^A{}_2L_4]^{2-}$ and $[Ln^B{}_2L_4]^{2-}$ was repetitively measured just after mixing (time = 0 minutes). If the hypothesis is correct, the two cages must have equal integrated area of the species isotopic pattern. From these integrated areas the relative amount of each species can be determined as follow:

$$\%[Ln^A Ln^B L_4] = \frac{A[Ln^A Ln^B L_4]}{\sum A[Ln^A Ln^B L_4]} \cdot 100 \qquad \text{eq. S2}$$

Where $\%[Ln^A Ln^B L_4]$ is the relative amount of the cage, and $A[Ln^A Ln^B L_4]$ is the integrated area of the species isotopic pattern (homonuclear $Ln^A = Ln^B$, heteronuclear $Ln^A \neq Ln^B$). The integrated area of the isotopic pattern was determined using ORIGIN 2021b software. Similar ionization efficiencies must give relative amounts of 50% for the $[Ln^A{}_2L_4]^{2-}$ and $[Ln^B{}_2L_4]^{2-}$ cages. In the case of the couple $[La_2L_4]^{2-}/[Lu_2L_4]^{2-}$, being the ion exchange kinetics very fast, the relative amount was determined after 30 minutes when the solution has reached the statistical mixture. In this case, the expected relative amounts for $[La_2L_4]^{2-}$, $[Lu_2L_4]^{2-}$ and $[LaLuL_4]^{2-}$ are 25%, 25% and 50%, respectively.

These experiments allow also to estimate the standard deviation (σ) of the measure. Table S4 shows the relative amounts determined from ESI-MS analyses for the couples $[Eu_2L_4]^{2-}/[Tb_2L_4]^{2-}$, $[Eu_2L_4]^{2-}/[Tm_2L_4]^{2-}$, $[Nd_2L_4]^{2-}/[Er_2L_4]^{2-}$ and $[La_2L_4]^{2-}/[Lu_2L_4]^{2-}$. Figure S11 reports an example of ESI-MS spectrum at time zero for the couples $[Eu_2L_4]^{2-}/[Tb_2L_4]^{2-}$, $[Eu_2L_4]^{2-}/[Tm_2L_4]^{2-}$ and $[Nd_2L_4]^{2-}/[Er_2L_4]^{2-}$ and after 30 minutes for the couple $[La_2L_4]^{2-}/[Lu_2L_4]^{2-}$.

Assuming that the total cages concentration remains constant at any time, it will be equal to the sum of the initial (t=0) concentrations of $[Ln^A{}_2L_4]^{2-}$ and $[Ln^B{}_2L_4]^{2-}$:

$$\sum |Ln^A Ln^B L_4|_t = \sum |Ln^A Ln^B L_4|_0 = |Ln^A_2 L_4|_0 + |Ln^B_2 L_4|_0 \qquad \text{eq. S3}$$

The relative amount (equation S2) can be expressed using the molar concentrations as follows:

$$\%[Ln^A Ln^B L_4] = \frac{|Ln^A Ln^B L_4|}{\sum |Ln^A Ln^B L_4|} \cdot 100 \qquad \text{eq. S4}$$

Combining equations S2 and S4, the molar concentration $|Ln^A Ln^B L_4|$ for a generic species at any time will be:

$$|Ln^A Ln^B L_4|_t = \frac{\%[Ln^A Ln^B L_4]\cdot \sum |Ln^A Ln^B L_4|_t}{100} = \frac{\%[Ln^A Ln^B L_4]\cdot \sum |Ln^A Ln^B L_4|_0}{100} = \\ = \frac{\%[Ln^A Ln^B L_4]\cdot (|Ln_2^A L_4|_0 + |Ln_2^B L_4|_0)}{100} \qquad \text{eq. S5}$$

where $Ln^A = Ln^B$ if the cage is homonuclear and $Ln^A \neq Ln^B$ if the cage is heteronuclear.

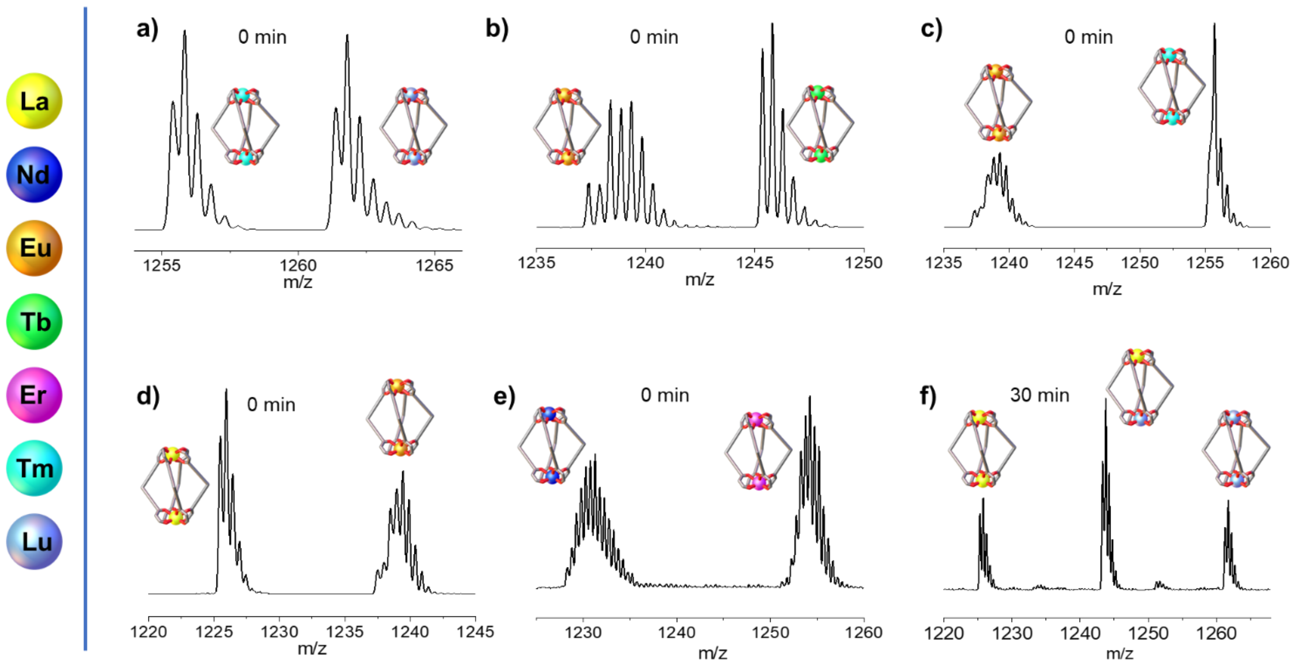

Figure S11 ESI-MS spectra at time zero for the couples a) $[Tm_2L_4]^{2-}/[Lu_2L_4]^{2-}$, b) $[Eu_2L_4]^{2-}/[Tb_2L_4]^{2-}$, c) $[Eu_2L_4]^{2-}/[Tm_2L_4]^{2-}$, d) $[La_2L_4]^{2-}/[Eu_2L_4]^{2-}$, e) $[Nd_2L_4]^{2-}/[Er_2L_4]^{2-}$ and f) after 30 minutes for the couple $[La_2L_4]^{2-}/[Lu_2L_4]^{2-}$.

Table S4 Relative amounts derived from the reproducibility experiments.

Measure # (time = 0 minutes)	**%$[Tm_2L_4]^{2-}$**	**%$[TmLuL_4]^{2-}$**	**%$[Lu_2L_4]^{2-}$**
1	50	0	50
2	49	0	51
3	51	0	49
4	51	0	49
5	48	0	52
σ	± 1.16	0	± 1.16
Measure # (time = 0 minutes)	**%$[Eu_2L_4]^{2-}$**	**%$[EuTbL_4]^{2-}$**	**%$[Tb_2L_4]^{2-}$**
1	51	0	49
2	50	0	50
3	48	0	52
4	51	0	49
5	49	0	51
σ	± 1.17	0	± 1.17
Measure # (time = 0 minutes)	**%$[Eu_2L_4]^{2-}$**	**%$[EuTmL_4]^{2-}$**	**%$[Tm_2L_4]^{2-}$**
1	49	0	51
2	50	0	50
3	49	0	51
4	50	0	50
5	51	0	49
σ	± 0.75	0	± 0.75
Measure # (time = 0 minutes)	**%$[La_2L_4]^{2-}$**	**%$[LaEuL_4]^{2-}$**	**%$[Eu_2L_4]^{2-}$**
1	51	0	49
2	51	0	49
3	52	0	48
4	48	0	52
5	49	0	51
σ	± 1.47	0	± 1.47
Measure # (time = 0 minutes)	**%$[Nd_2L_4]^{2-}$**	**%$[NdErL_4]^{2-}$**	**%$[Er_2L_4]^{2-}$**
1	49	0	51
2	51	0	49
3	52	0	48
4	48	0	52
5	51	0	49
σ	± 1.45	0	± 1.45
Measure # (time = 30 minutes)	**%$[La_2L_4]^{2-}$**	**%$[LaLuL_4]^{2-}$**	**%$[Lu_2L_4]^{2-}$**
1	24	50	26
2	24	53	23
3	25	51	24
4	23	53	24
5	26	49	25
σ	± 1.02	± 1.60	± 1.02

6. Ln ion dynamic exchange and time-dependent ESI-MS

Two stoke equimolar solutions of $[Ln^{A}_2L_4]^{2-}$ and $[Ln^{B}_2L_4]^{2-}$ were prepared in acetonitrile. Equal aliquots of the two solutions were taken and mixed (final concentration of each cage 10^{-5} M) in a screw capped vial, and placed in an oven at 50 °C. An aliquot of this solution was taken at different times, diluted to 10^{-6} M and analysed by ESI-MS. Equation S1 was used to determine the relative cage amount from the integrated area of the species isotopic pattern and equation S4 to calculate the species molarity.

7. Kinetic analysis of the dynamic Ln ion exchange

Some previous works[11–13] treated the kinetics of dynamic exchange between metallo-supramolecular architectures as direct reactions without considering the reversible nature of the equilibrium. When collecting data for kinetic analysis, itis to not follow the kinetics over a longer time such as several half-lives for direct reactions or times close to or even higher the equilibration time for reversible reactions.[14] Ignoring these data at longer times can lead to apparent satisfactory modelling of the experimental data with rate integrated laws of first- or second-order direct reactions. Thus, misleading information such as wrong kinetic constant value or, even worst, wrong reaction order are obtained. For instance, let consider the concentration variation of the $[Eu_2L_4]^{2-}$ cage in the ion exchange between $[Eu_2L_4]^{2-}$ and $[Tb_2L_4]^{2-}$. Avoiding to include experimental data close to equilibrium (red points of Figure S12a) leads to a satisfactory fitting either using the integrated law of a direct first-order reaction (Figure S12b, $R^2 = 0.97$) or the integrated law of a direct second-order reaction (Figure S12c, $R^2 = 0.99$). However, data close to the equilibration time (red points) are clearly out the linear fitting in both cases.

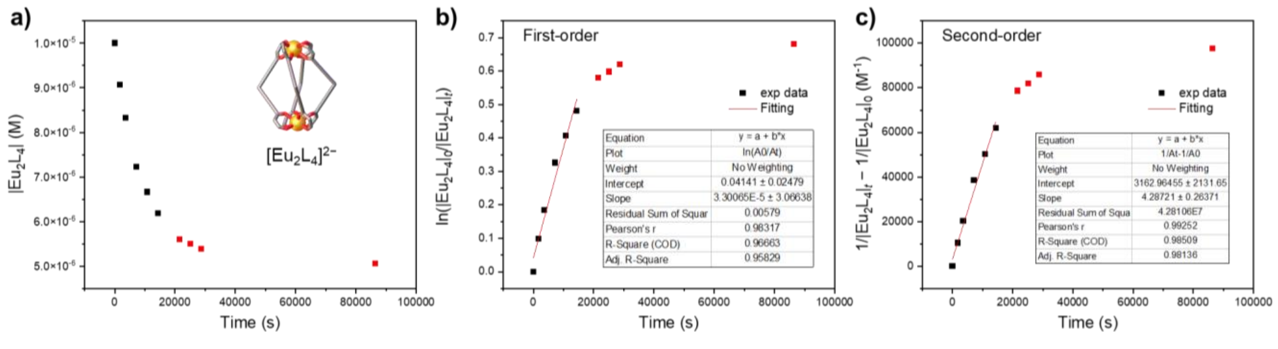

Figure S12 a) Concentration over time of $[Eu_2L_4]^{2-}$ during the dynamic Ln ion exchange between $[Eu_2L_4]^{2-}$ and $[Tb_2L_4]^{2-}$, red points indicate a $[Eu_2L_4]^{2-}$ concentration up to 10% higher than equilibrium concentration. Wrong data elaboration with (b) first-order ($R^2 = 0.97$) and (c) second-order integrated laws ($R^2 = 0.99$), red points not considered for the linear fittings.

As a matter of fact, the dynamic Ln ion exchange reaction (eq. S6) is a reversible reaction and its kinetics must be treated as a pair of forward and backward reactions (kinetic constants k_f and k_b, respectively) that occur simultaneously and related to the equilibrium constant K by eq. S7. Only if $k_f \gg k_b$ (high value for K), the reverse reaction can be neglected, and the kinetics analysis simplifies to a rate law of a direct reaction. However, this is not the case. Since the exchange equilibrium leads to a statistical mixture of two homometallic cages and one heterometallic cage with a ratio 1:1:2, it is trivial to demonstrate that $K = 4$. Hence, k_b will be one quarter of k_f and the backward reaction cannot be neglected.

$[Ln^A{}_2L_4]^{2-} + [Ln^B{}_2L_4]^{2-} \rightleftharpoons 2\,[Ln^ALn^BL_4]^{2-}$ eq. S6

$K = k_f / k_b$ eq. S7

$$[Ln^A{}_2L_4]^{2-} + [Ln^B{}_2L_4]^{2-} \underset{k_b}{\overset{k_f}{\rightleftharpoons}} [Ln^ALn^BL_4]^{2-} \quad \text{eq. S8}$$

t_0	a_0	a_0	0
t	$a_0 - x$	$a_0 - x$	$2x$

where a_0 is the initial concentration of the homometallic cages and the consumed and formed species are indicated with x.

The rates of the forward and backward reactions are r_f and r_b:

$r_f = k_f\,|Ln^A{}_2L_4||Ln^B{}_2L_4| = k_f(a_0 - x)^2$ eq. S9

$r_b = k_b\,|Ln^ALn^BL_4|^2 = k_b(2x)^2$ eq. S10

Hence, dx/dt will be:

$dx/dt = k_f(a_0 - x)^2 - k_b 4x^2$ eq. S11

At the equilibrium $r_f = r_b$ and hence the eq. S11 becomes:

$k_f(a_0 - x_{eq})^2 = k_b 4x_{eq}{}^2$ eq. S12

where x_{eq} is the concentration variation at the equilibrium. Using eq. S12 to derive k_b as a function of k_f and substituting in eq. S11, we obtain:

$$\frac{dx}{dt} = k_f\left[(a_0 - x)^2 - \frac{(a_0 - x_{eq})^2}{4x_{eq}^2}4x^2\right] \quad \text{eq. S13}$$

Rearranging eq. S13, we get:

$$\frac{dx}{dt} = k_f\frac{(a_0^2x_{eq}^2 + 2a_0x^2x_{eq} - a_0^2x^2 - 2a_0x_{eq}^2x)}{x_{eq}^2} \quad \text{eq. S14}$$

Integration[14] of eq. S14 gives:

$$k_f t = \frac{x_{eq}}{2a_0(a_0 - x_{eq})} ln\frac{x(a_0 - 2x_{eq}) + a_0x_{eq}}{a_0(x_{eq} - x)} \quad \text{eq. S15}$$

Eq. S15 can be rearranged to eq. S16:

$$e^{\left[\frac{k_f t 2a_0(a_0 - x_{eq})}{x_{eq}}\right]} = \frac{x(a_0 - 2x_{eq}) + a_0 x_{eq}}{a_0(x_{eq} - x)} \qquad \text{eq. S16}$$

In the specific case here discussed, at the equilibrium when the statistical mixture is reached the concentration of the homometallic cages are $a_{eq} = a_0/2$ and hence $x_{eq} = a_0/2$. Substituting in eq. S16 we obtain:

$$x = \frac{a_0}{2}(1 - e^{-k_f t 2a_0}) \qquad \text{eq. S17}$$

Since the concentration of the homometallic cages $[Ln^A{}_2L_4]^{2-}$ and $[Ln^A{}_2L_4]^{2-}$ is $(a_0 - x)$ and the concentration of the heterometallic cage $[Ln^ALn^BL_4]^{2-}$ is $2x$, substituting in eq. S17 we obtain:

$$|Ln_2^A L_4| = |Ln_2^B L_4| = \frac{a_0}{2}(1 + e^{-k_f t 2a_0}) \qquad \text{eq. S18}$$

$$|Ln^A Ln^B L_4| = a_0(1 - e^{-k_f t 2a_0}) \qquad \text{eq. S19}$$

Fitting of experimental data (Figure 5 and Figures S15-S17, S20-S22, S25-S27, S30-S32) with eq. S18 and S19 allow to determine the k_f value and then the k_b from eq. S7.

Moreover, the kinetic analysis above performed can be used also to estimate t_{eq}, the time to reach the equilibrium (*i.e.* the statistical mixture). At the equilibrium $x = x_{eq}$, but substituting this value in eq. S15 the expression assumes no meaning. Hence, we can take into consideration the situation just before the complete equilibration. Remembering that the concentration of the homometallic cage at equilibrium is $a_{eq} = a_0/2$, we get:

$$a = a_{eq} + \alpha a_{eq} = \frac{a_0}{2} + \alpha\frac{a_0}{2} \qquad \text{eq. S20}$$

where α is a small number. Hence by considering that $a = a_0 - x$, x becomes:

$$x = \frac{a_0}{2}(1 - \alpha) \qquad \text{eq. S21}$$

Substituting in eq. S15 we obtain:

$$t_{eq} = \frac{1}{2a_0 k_f} ln\frac{1}{\alpha} \qquad \text{eq. S22}$$

For calculation of t_{eq}, we arbitrary assumed $\alpha = 0.01$, that corresponds to a homometallic cage concentration a that is 1% higher than the equilibrium concentration, then a situation just before the complete equilibration.

7.1 Ln ion exchange kinetics for $[Tm_2L_4]^{2-}$/$[Lu_2L_4]^{2-}$ (ΔEIR = 0.02 Å)

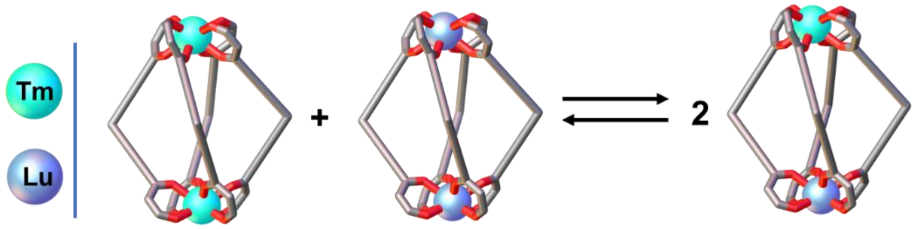

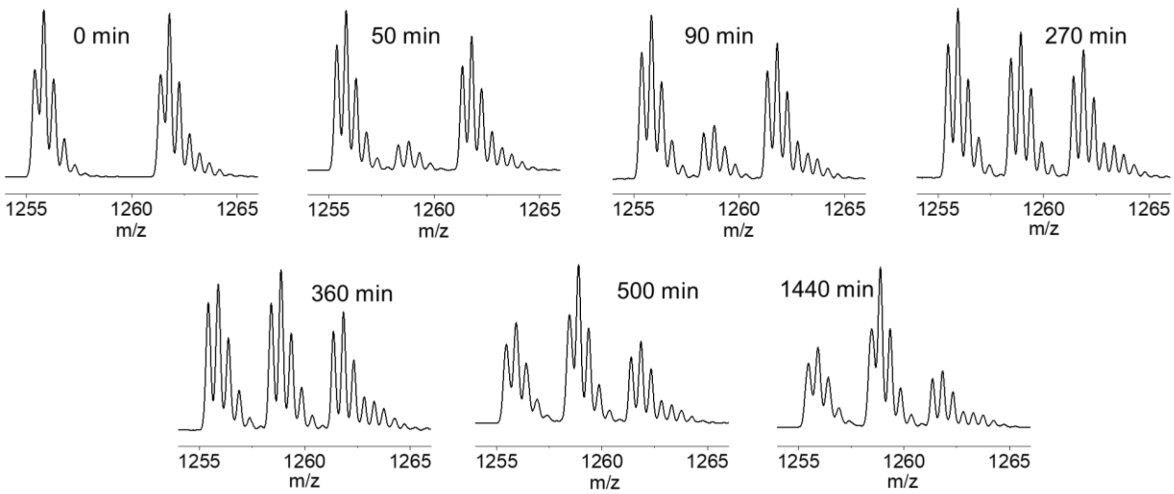

Figure S13 Time dependent ESI-MS spectra of ion exchange for $[Tm_2L_4]^{2-}$/$[Lu_2L_4]^{2-}$.

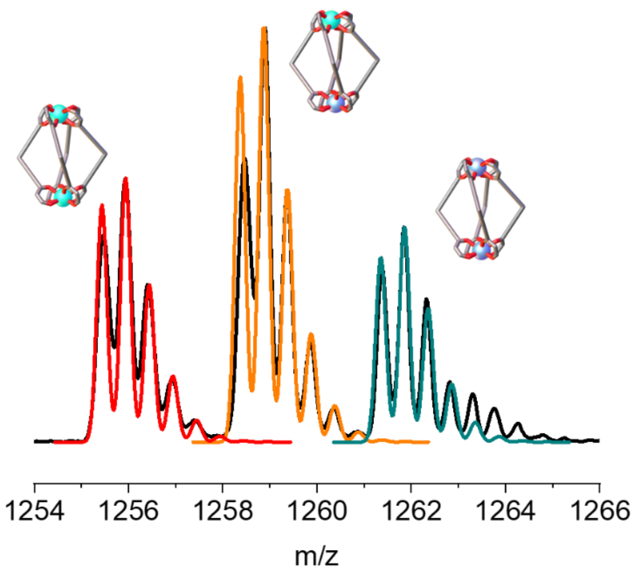

Figure S14 Experimental data, black line, and simulated patterns for $[Tm_2L_4]^{2-}$, red line, for $[Lu_2L_4]^{2-}$, green line, and for $[TmLuL_4]^{2-}$, orange line after 1440 minutes.

Table S5 Relative amounts for $[Tm_2L_4]^{2-}$/$[Lu_2L_4]^{2-}$ ion exchange derived from ESI-MS.

Time (min)	%$[Tm_2L_4]^{2-}$	%$[TmLuL_4]^{2-}$	%$[Lu_2L_4]^{2-}$
0	49.8	0	50.2
50	45.5	8.7	45.7
90	42.8	14.6	42.6
270	33.8	32.3	33.9
360	31.3	37.5	31.3
500	28.5	42.7	28.8
1440	24.9	49.8	25.1

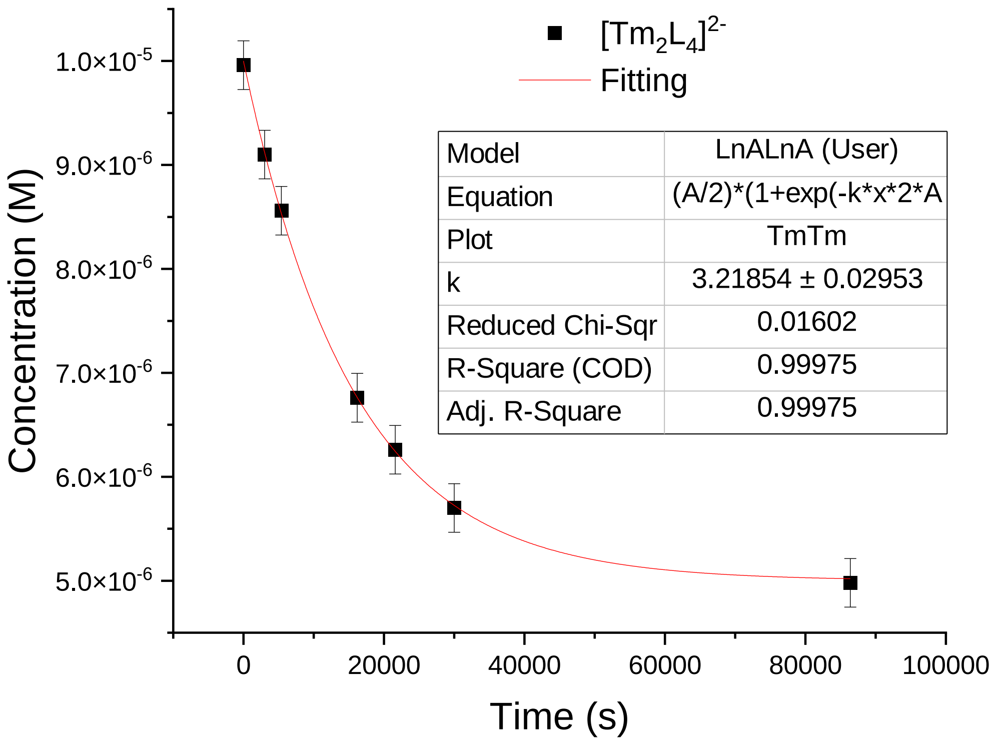

Figure S15 $[Tm_2L_4]^{2-}$ concentration over time during the $[Tm_2L_4]^{2-}$/$[Lu_2L_4]^{2-}$ ion exchange derived from ESI-MS.

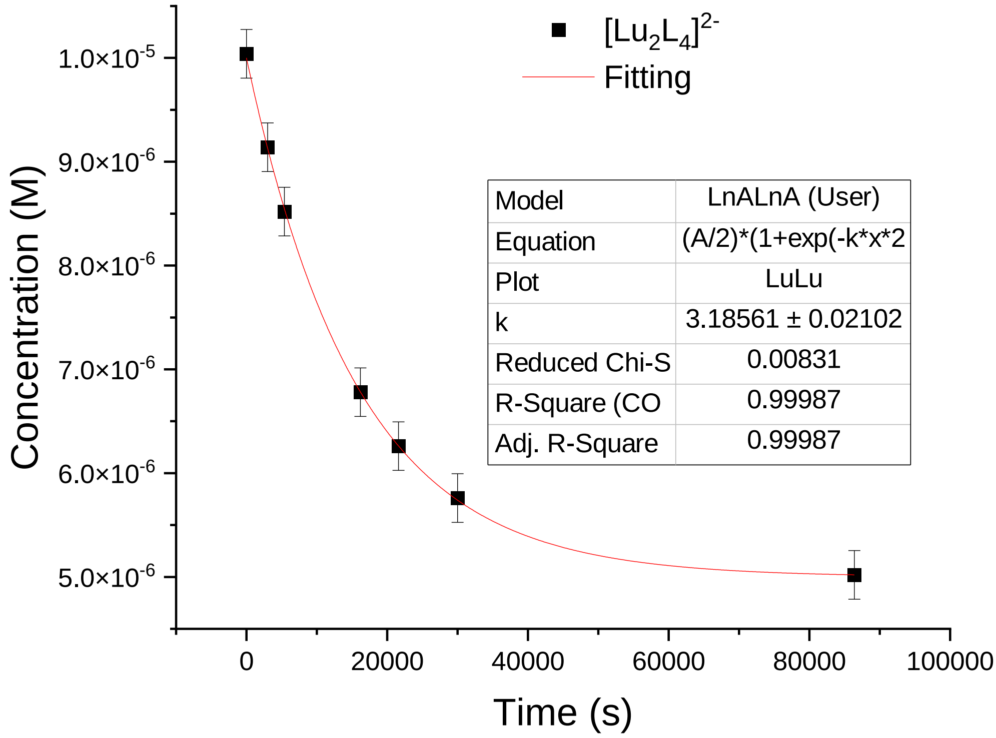

Figure S16 $[Lu_2L_4]^{2-}$ concentration over time during the $[Tm_2L_4]^{2-}/[Lu_2L_4]^{2-}$ ion exchange derived from ESI-MS.

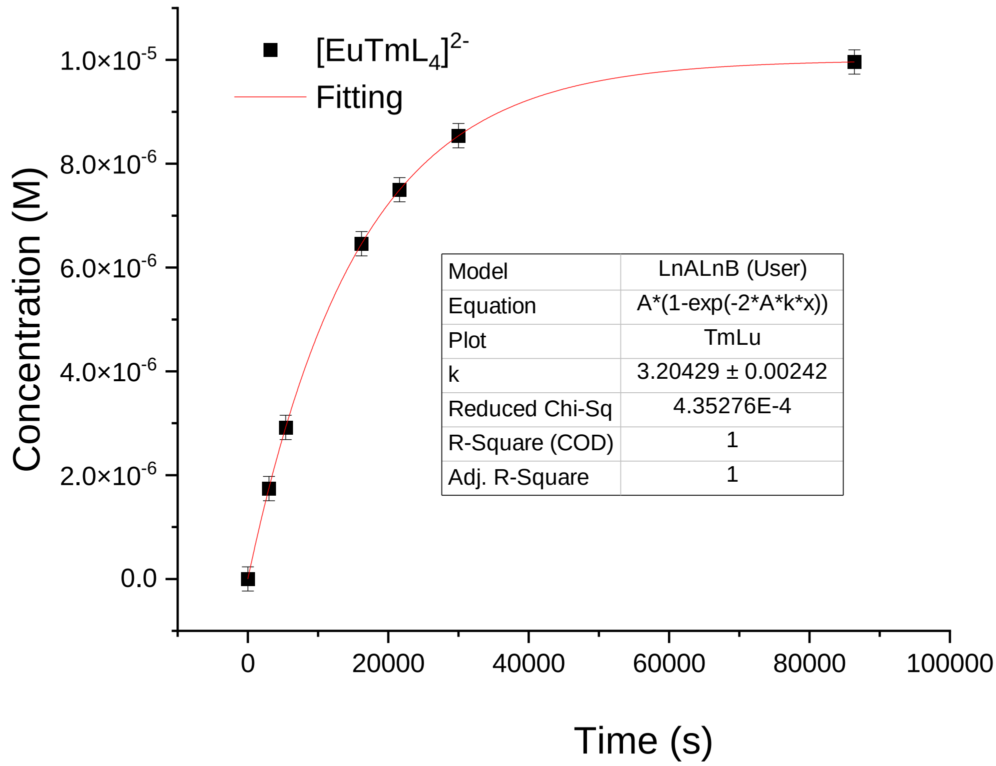

Figure S17 $[TmLuL_4]^{2-}$ concentration over time during the $[Tm_2L_4]^{2-}/[Lu_2L_4]^{2-}$ ion exchange derived from ESI-MS.

7.2 Ln ion exchange kinetics for $[Eu_2L_4]^{2-}$/$[Tb_2L_4]^{2-}$ (ΔEIR = 0.03 Å)

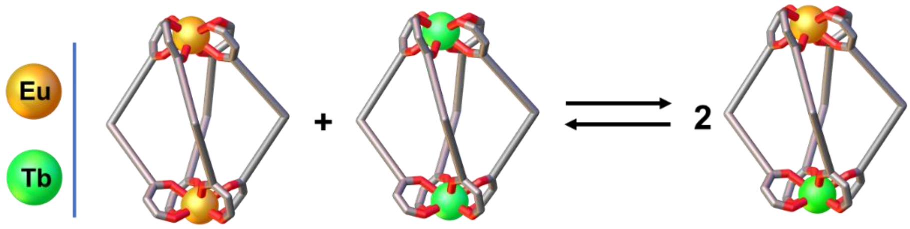

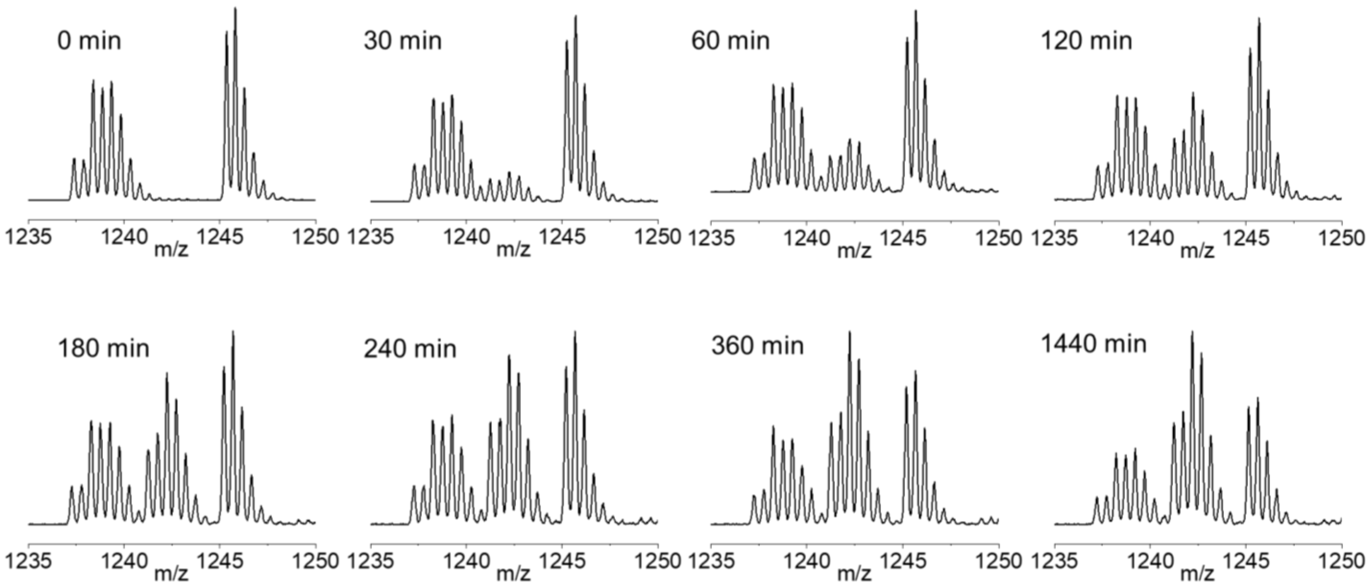

Figure S18 Time dependent ESI-MS spectra of ion exchange for $[Eu_2L_4]^{2-}$/$[Tb_2L_4]^{2-}$.

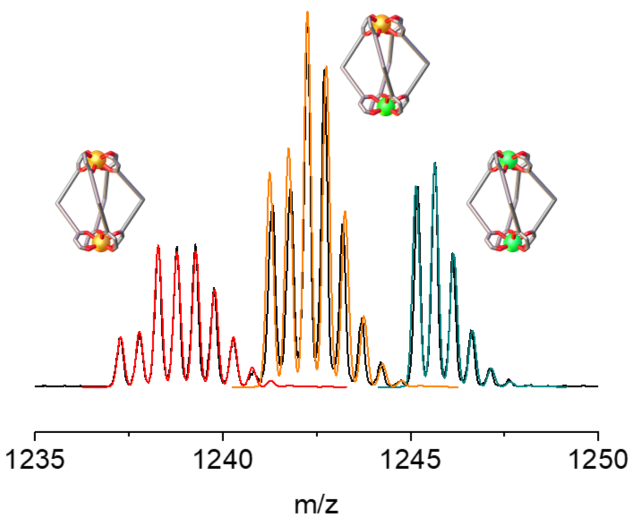

Figure S19 Experimental data, black line, and simulated patterns for $[Eu_2L_4]^{2-}$, red line, for $[Tb_2L_4]^{2-}$, green line, and for $[EuTbL_4]^{2-}$, orange line after 1440 minutes.

Table S6 Relative amounts for $[Eu_2L_4]^{2-}$/$[Tb_2L_4]^{2-}$ ion exchange derived from ESI-MS.

Time (min)	%$[Eu_2L_4]^{2-}$	%$[EuTbL_4]^{2-}$	%$[Tb_2L_4]^{2-}$
0	50.1	0	49.9
30	45.3	10.2	44.5
60	41.6	17.2	41.2
120	36.1	28.1	35.7
180	33.3	34.7	32.0
240	30.9	39.0	30.1
360	28.0	44.2	27.8
420	27.1	46.0	26.9
480	26.4	47.3	26.3
1440	25.3	49.9	24.8

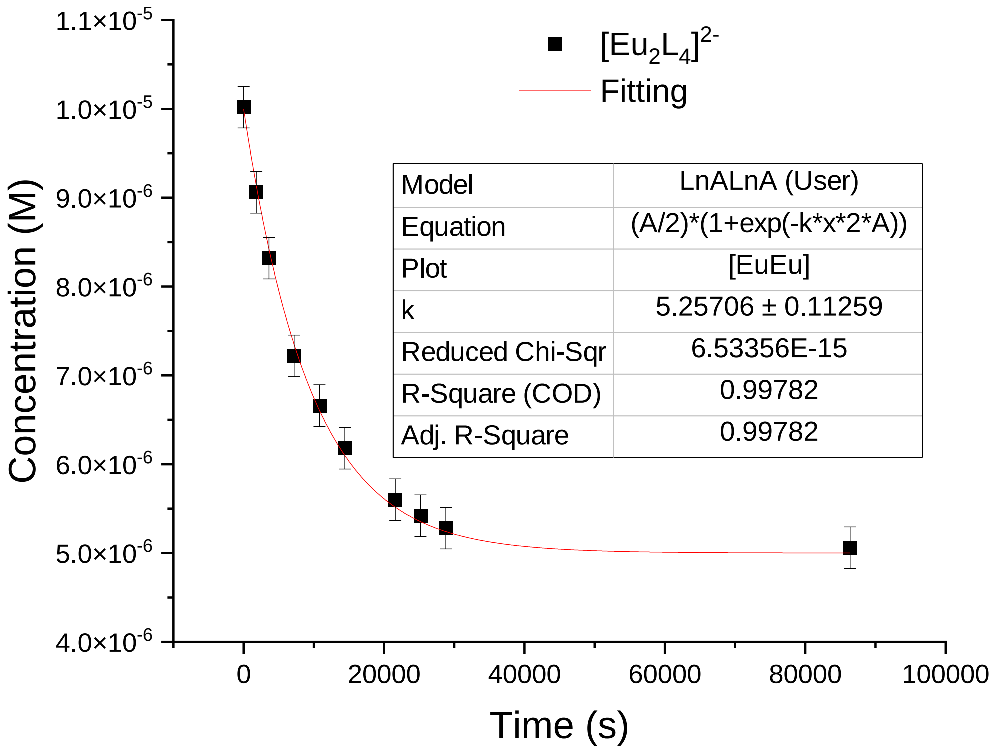

Figure S20 $[Eu_2L_4]^{2-}$ concentration over time during the $[Eu_2L_4]^{2-}$/$[Tb_2L_4]^{2-}$ ion exchange derived from ESI-MS.

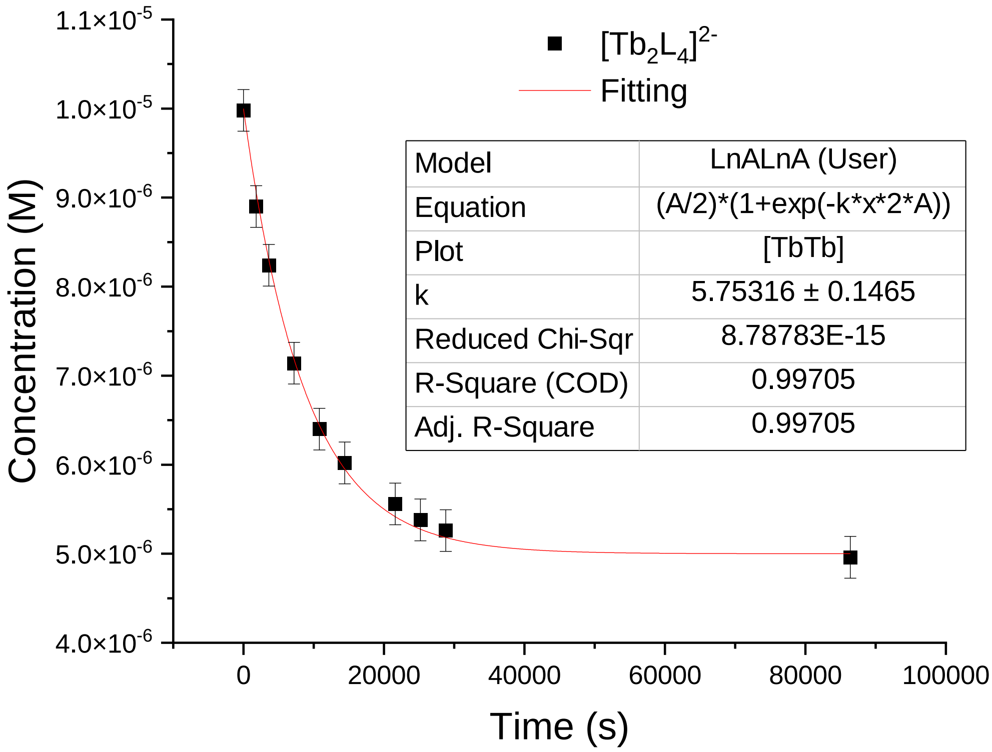

Figure S21 $[Tb_2L_4]^{2-}$ concentration over time during the $[Eu_2L_4]^{2-}$/$[Tb_2L_4]^{2-}$ ion exchange derived from ESI-MS.

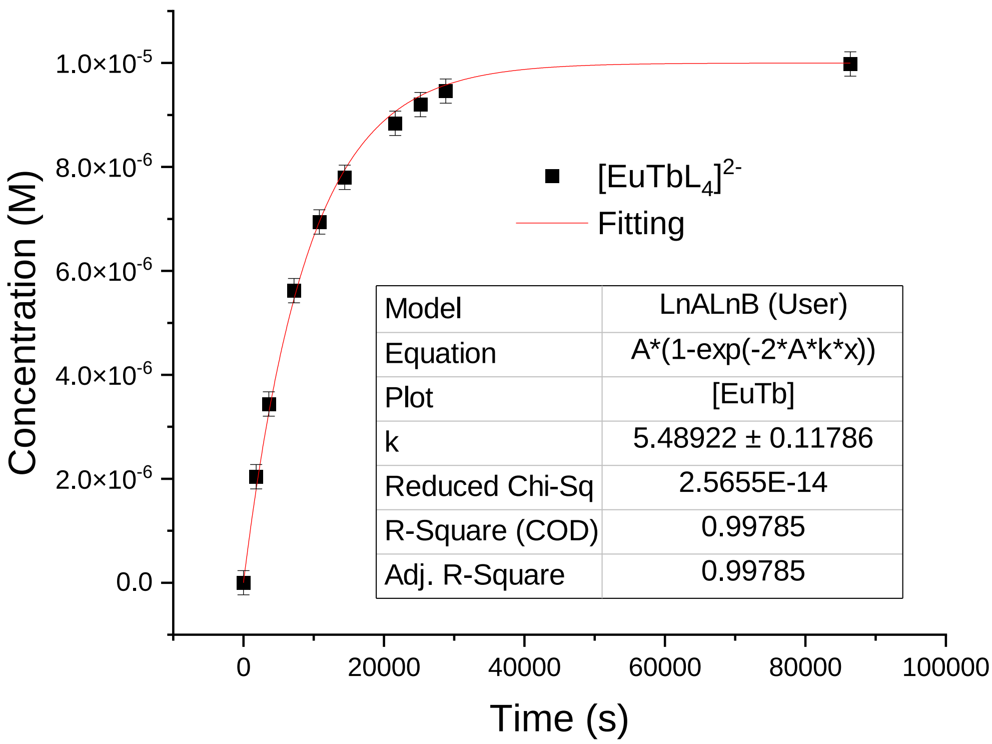

Figure S22 $[EuTbL_4]^{2-}$ concentration over time during the $[Eu_2L_4]^{2-}$/$[Tb_2L_4]^{2-}$ ion exchange derived from ESI-MS.

7.3 Ln ion exchange kinetics for $[Eu_2L_4]^{2-}$/$[Tm_2L_4]^{2-}$ (ΔEIR = 0.08 Å)

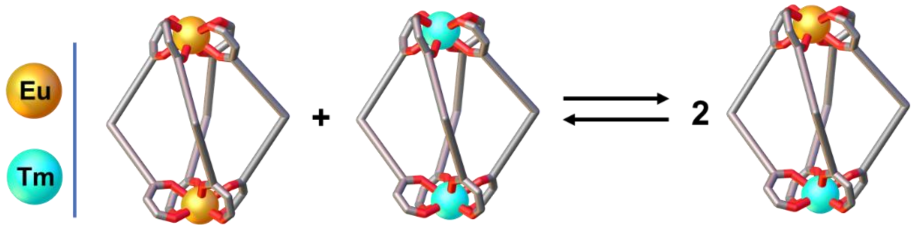

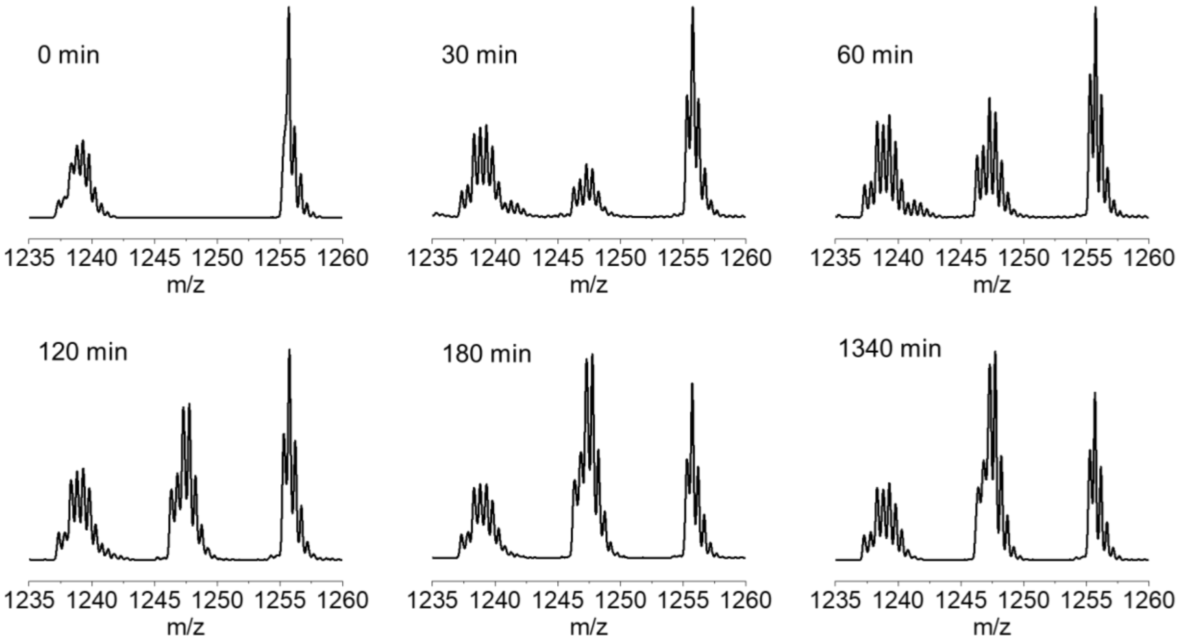

Figure S23 Time dependent ESI-MS spectra of ion exchange for $[Eu_2L_4]^{2-}$/$[Tm_2L_4]^{2-}$.

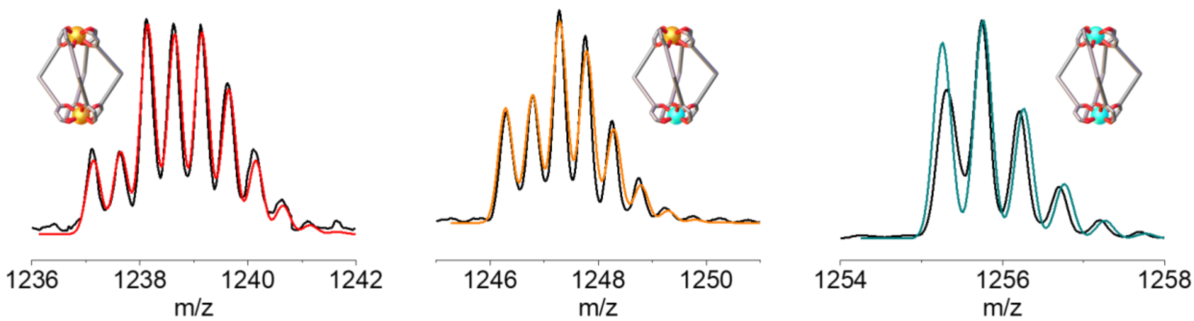

Figure S24 Experimental data black line, simulated patterns for $[Eu_2L_4]^{2-}$ red line, for $[EuTmL_4]^{2-}$ orange line and for $[Tm_2L_4]^{2-}$ green line after 60 minutes.

Table S7 Relative amounts for $[Eu_2L_4]^{2-}$/$[Tm_2L_4]^{2-}$ ion exchange derived from ESI-MS.

Time (min)	%$[Eu_2L_4]^{2-}$	%$[EuTmL_4]^{2-}$	%$[Tm_2L_4]^{2-}$
0	50.1	0	49.1
30	40.1	21.2	39.3
60	35.5	29.8	34.7
120	30.5	39.3	30.2
180	25.9	48.0	26.1
1340	24.9	50.4	24.7

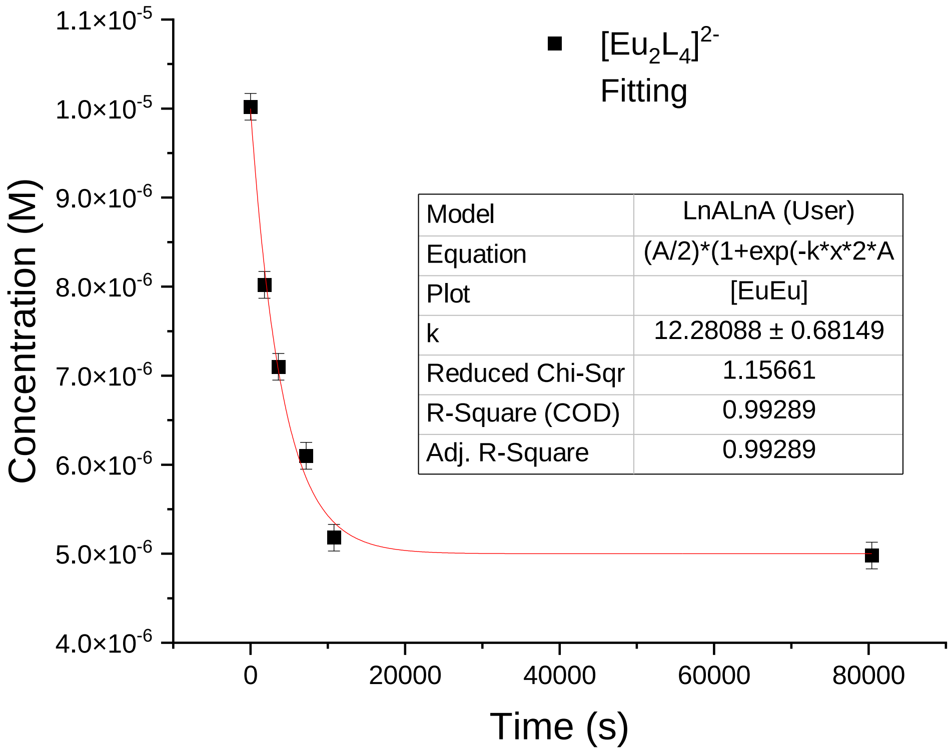

Figure S25 $[Eu_2L_4]^{2-}$ concentration over time during the $[Eu_2L_4]^{2-}$/$[Tm_2L_4]^{2-}$ ion exchange derived from ESI-MS.

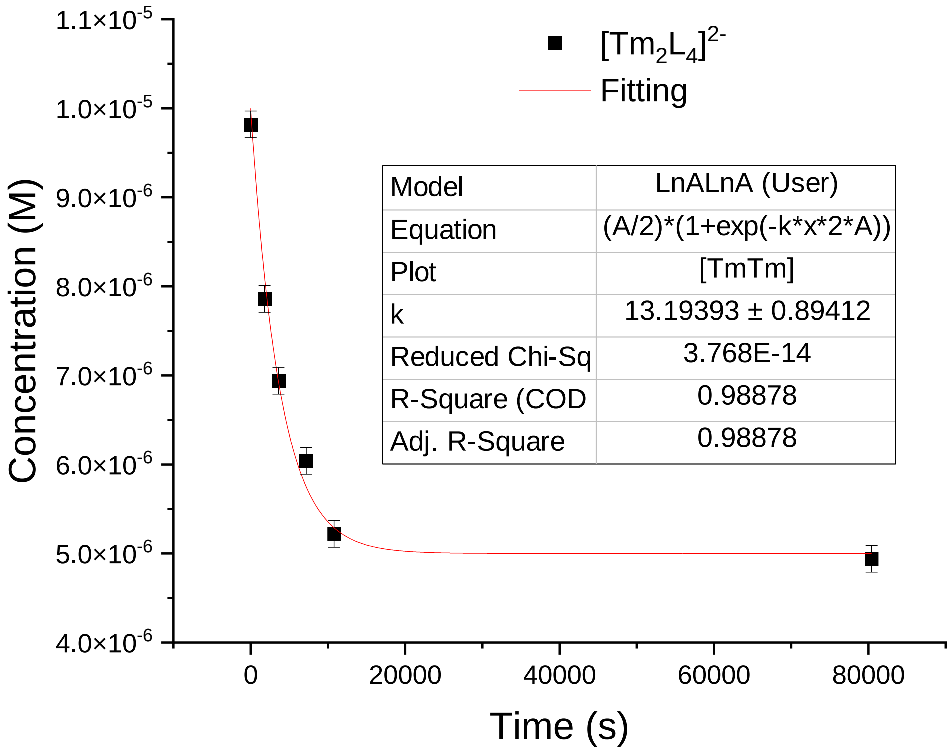

Figure S26 $[Tm_2L_4]^{2-}$ concentration over time during the $[Eu_2L_4]^{2-}$/$[Tm_2L_4]^{2-}$ ion exchange derived from ESI-MS.

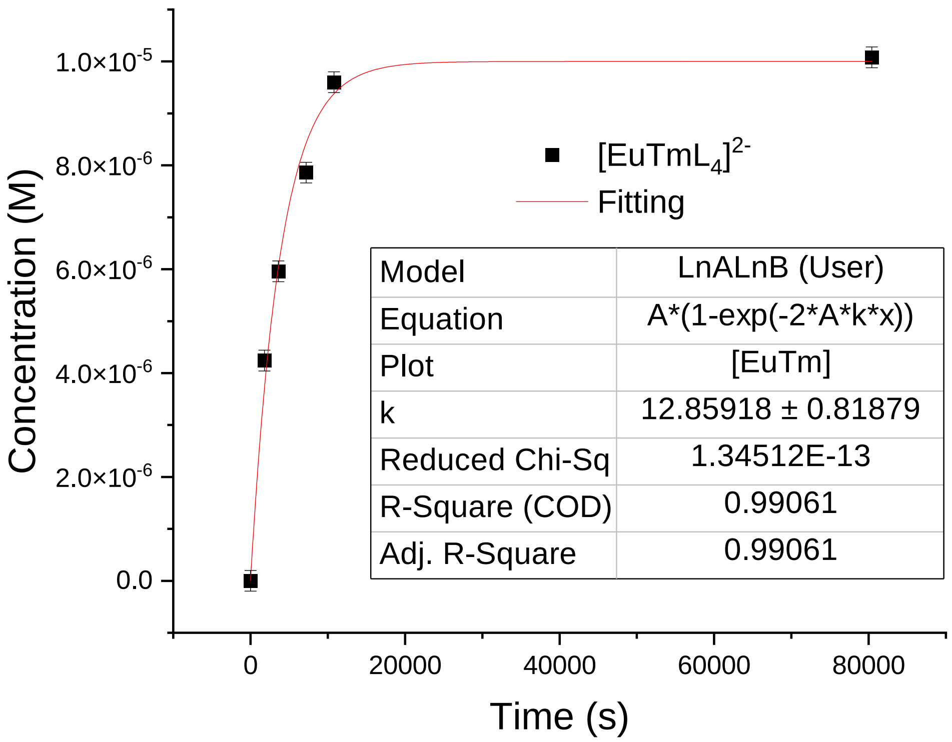

Figure S27 $[EuTmL_4]^{2-}$ concentration over time during the $[Eu_2L_4]^{2-}$/$[Tm_2L_4]^{2-}$ ion exchange derived from ESI-MS.

7.4 Ln ion exchange kinetics for $[La_2L_4]^{2-}$/$[Eu_2L_4]^{2-}$ (ΔEIR = 0.11 Å)

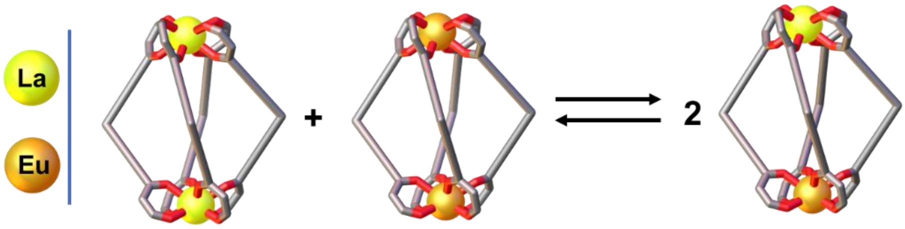

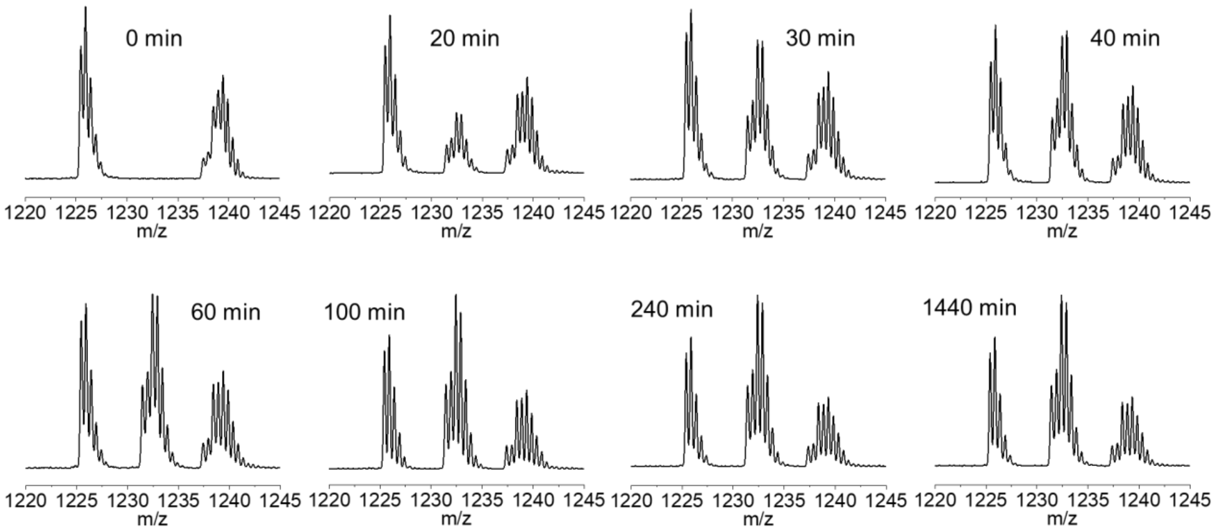

Figure S28 Time dependent ESI-MS spectra of ion exchange for $[La_2L_4]^{2-}$/$[Eu_2L_4]^{2-}$.

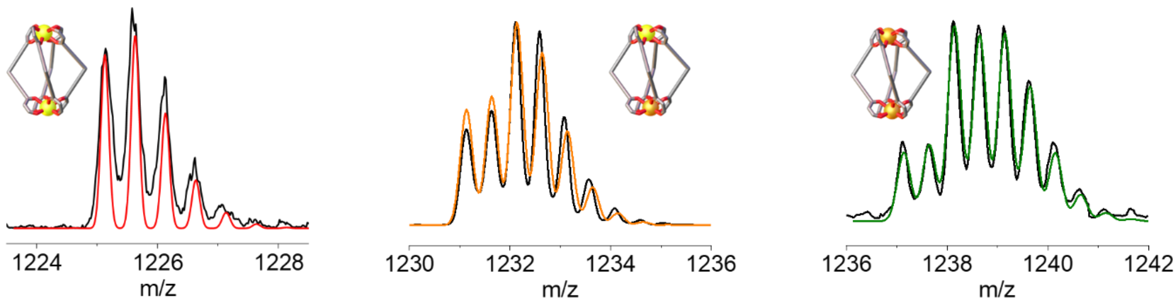

Figure S29 Experimental data black line, simulated patterns for $[La_2L_4]^{2-}$ red line, for $[LaEuL_4]^{2-}$ orange line and for $[Eu_2L_4]^{2-}$ green line after 40 minutes.

Table S8 Relative amounts for $[La_2L_4]^{2-}$/$[Eu_2L_4]^{2-}$ ion exchange derived from ESI-MS.

Time (min)	**%$[La_2L_4]^{2-}$**	**%$[LaEuL_4]^{2-}$**	**%$[Eu_2L_4]^{2-}$**
0	50	0	50
20	39.2	21.5	39.2
30	31.8	36.0	32.2
40	29.8	40.4	29.8
60	28.4	43.3	28.3
100	26.4	47.1	26.5
240	25.3	49.3	25.3
1440	25.1	49.9	25.0

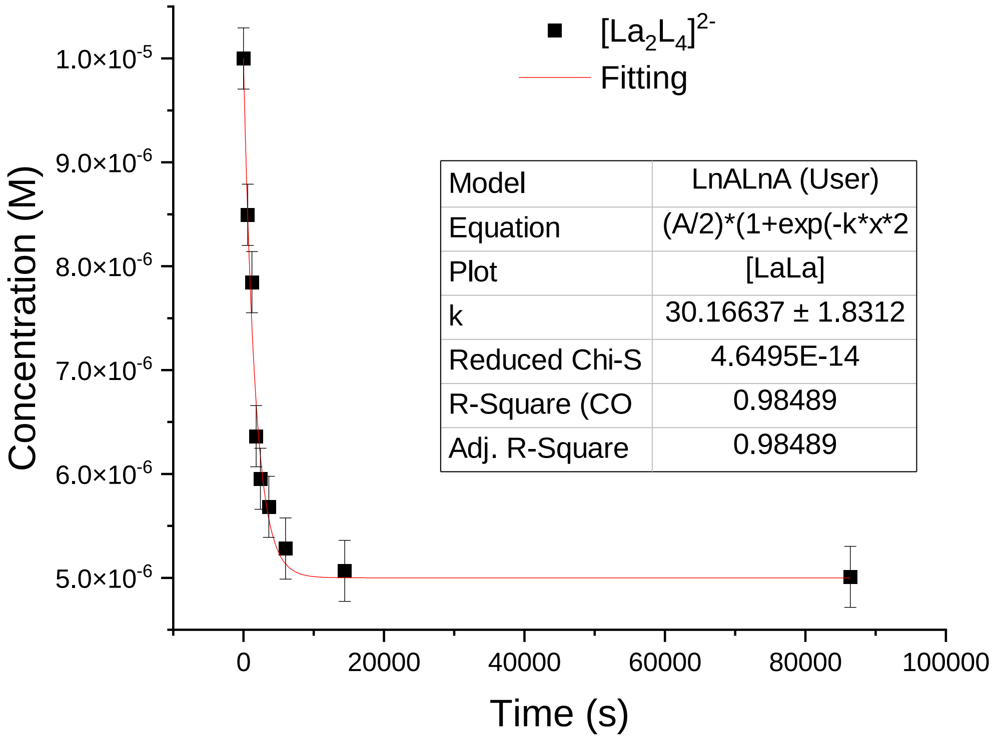

Figure S30 $[La_2L_4]^{2-}$ concentration over time during the $[La_2L_4]^{2-}$/$[Eu_2L_4]^{2-}$ ion exchange derived from ESI-MS.

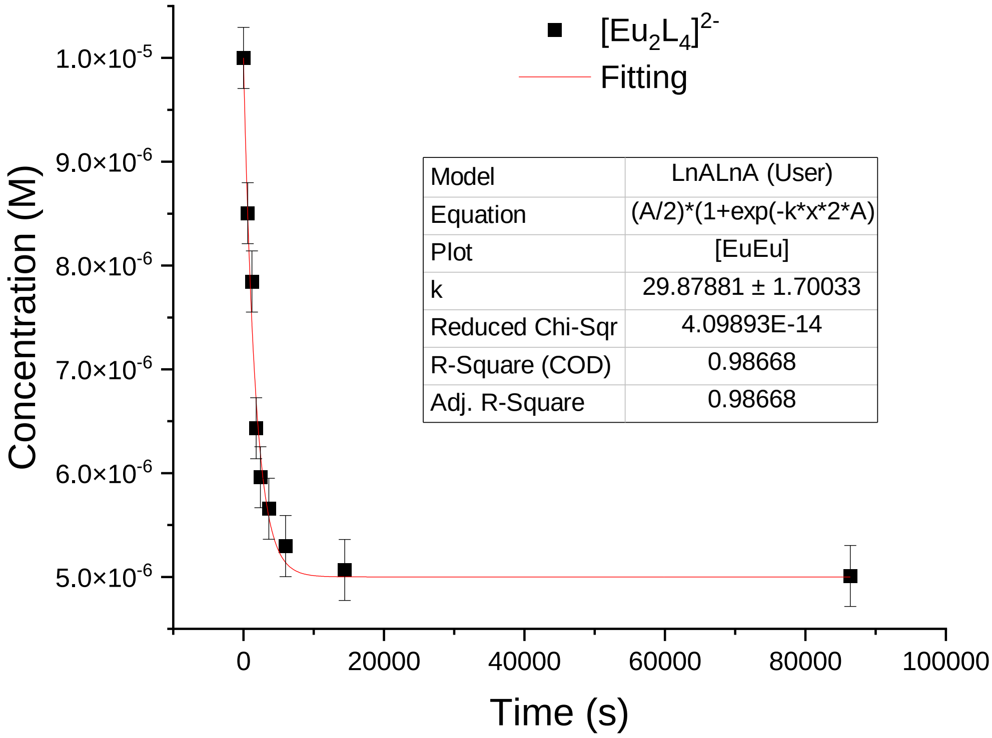

Figure S31 $[Eu_2L_4]^{2-}$ concentration over time during the $[La_2L_4]^{2-}$/$[Eu_2L_4]^{2-}$ ion exchange derived from ESI-MS.

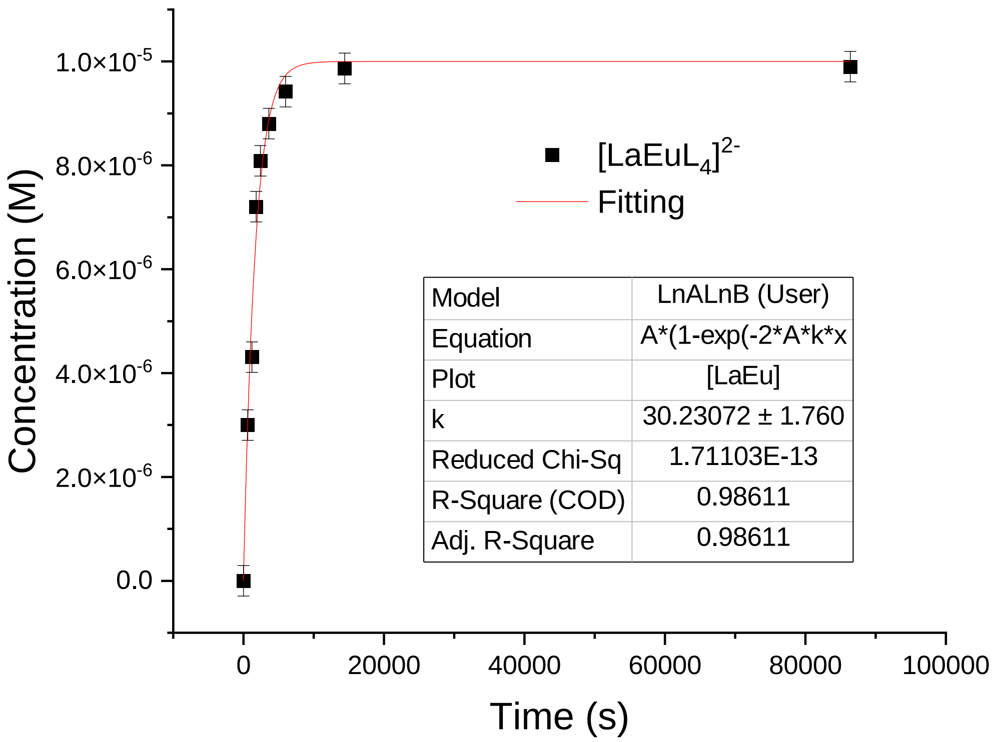

Figure S32 $[LaEuL_4]^{2-}$ concentration over time during the $[La_2L_4]^{2-}$/$[Eu_2L_4]^{2-}$ ion exchange derived from ESI-MS.

7.5 Ln ion exchange kinetics for $[Nd_2L_4]^{2-}$/$[Er_2L_4]^{2-}$ (ΔEIR = 0.12 Å)

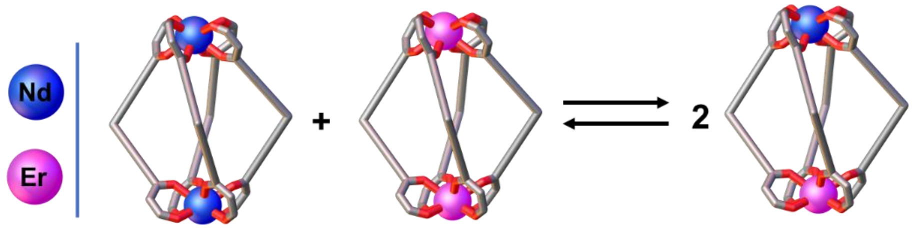

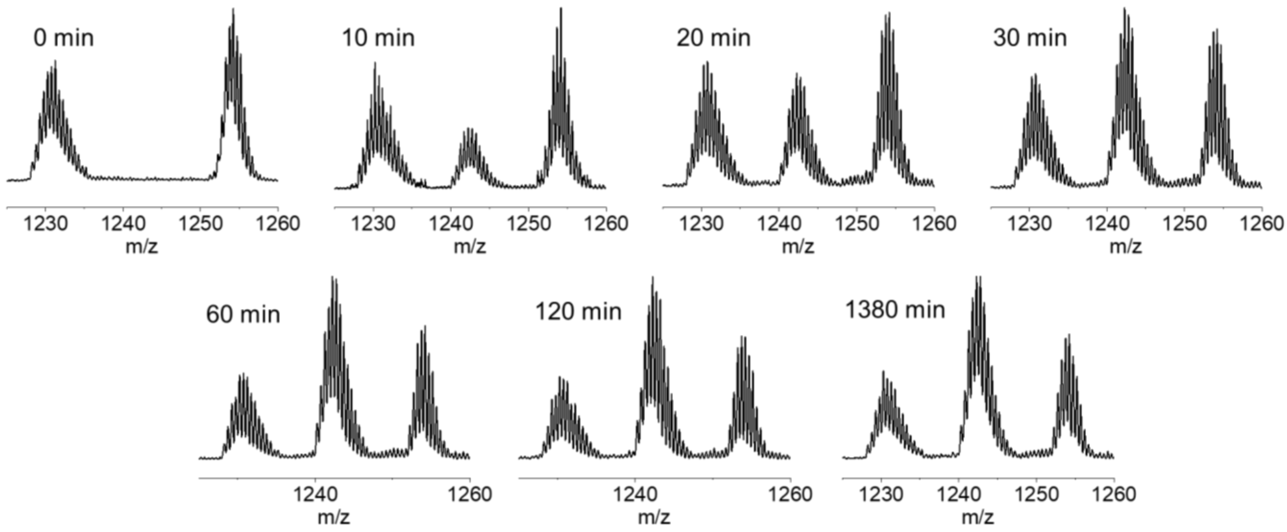

Figure S33 Time dependent ESI-MS spectra of ion exchange for $[Nd_2L_4]^{2-}$/$[Er_2L_4]^{2-}$.

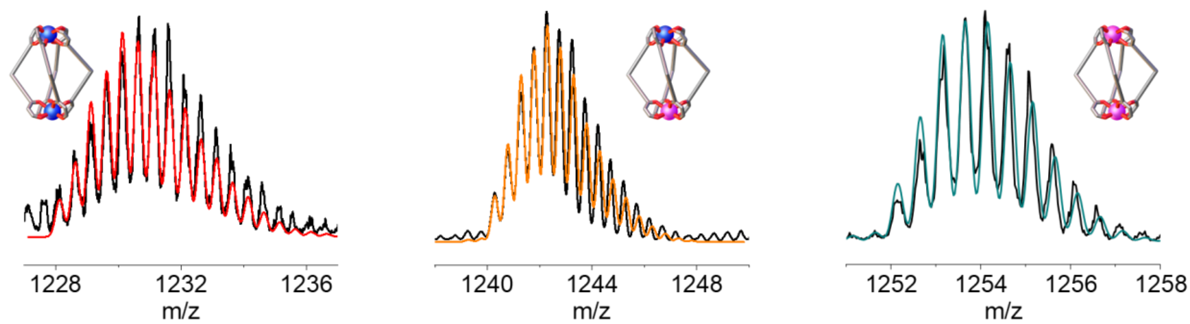

Figure S34 Experimental data black line, simulated patterns for $[Nd_2L_4]^{2-}$ red line, for $[NdErL_4]^{2-}$ orange line and for $[Er_2L_4]^{2-}$ green line after 1380 minutes.

Table S9 Relative amounts for $[Nd_2L_4]^{2-}$/$[Er_2L_4]^{2-}$ ion exchange derived from ESI-MS.

Time (min)	%$[Nd_2L_4]^{2-}$	%$[NdErL_4]^{2-}$	%$[Er_2L_4]^{2-}$
1	49.9	0.2	49.8
10	40.1	20.8	39.1
20	35.2	29.4	35.4
30	29.0	41.9	29.1
60	25.3	48.8	25.9
120	25.9	48.6	25.5
1380	25.1	50.0	24.9

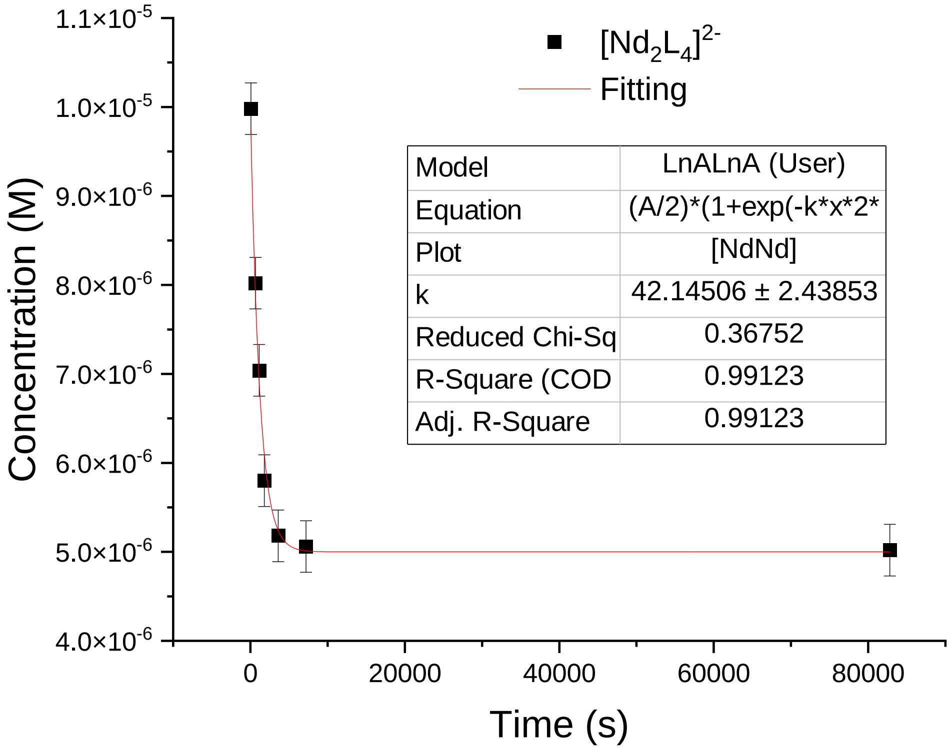

Figure S35 $[Nd_2L_4]^{2-}$ concentration over time during the $[Nd_2L_4]^{2-}$/$[Er_2L_4]^{2-}$ ion exchange derived from ESI-MS.

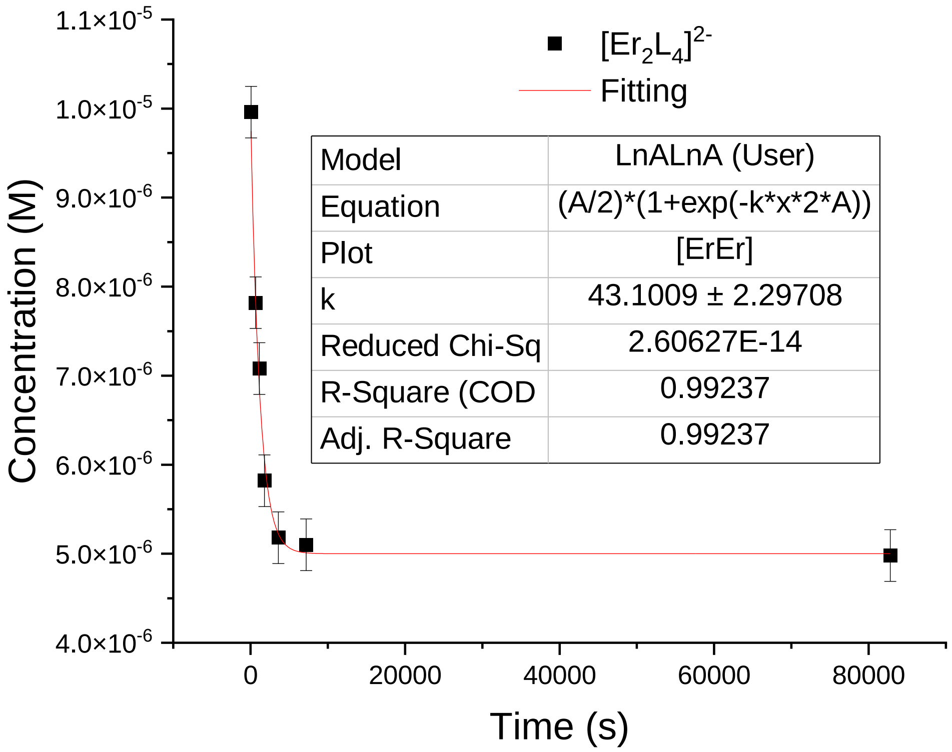

Figure S36 $[Er_2L_4]^{2-}$ concentration over time during the $[Nd_2L_4]^{2-}$/$[Er_2L_4]^{2-}$ ion exchange derived from ESI-MS.

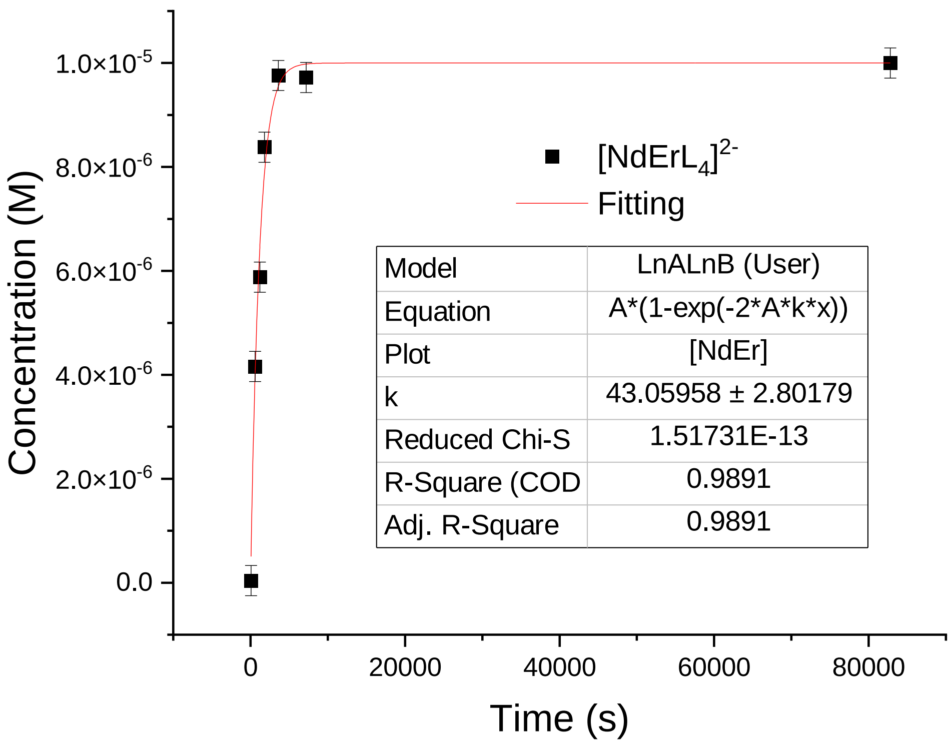

Figure S37 $[NdErL_4]^{2-}$ concentration over time during the $[Nd_2L_4]^{2-}$/$[Er_2L_4]^{2-}$ ion exchange derived from ESI-MS.

7.6 Ln ion exchange kinetics for $[La_2L_4]^{2-}$/$[Lu_2L_4]^{2-}$ (ΔEIR = 0.21 Å)

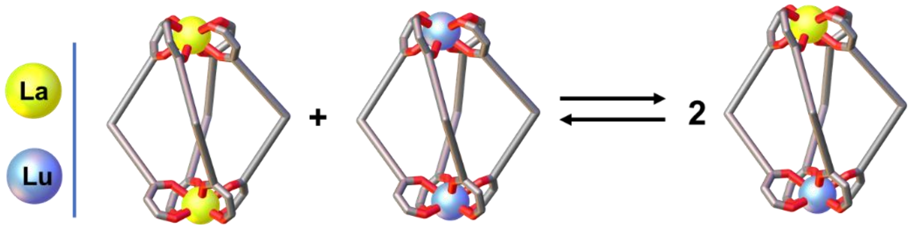

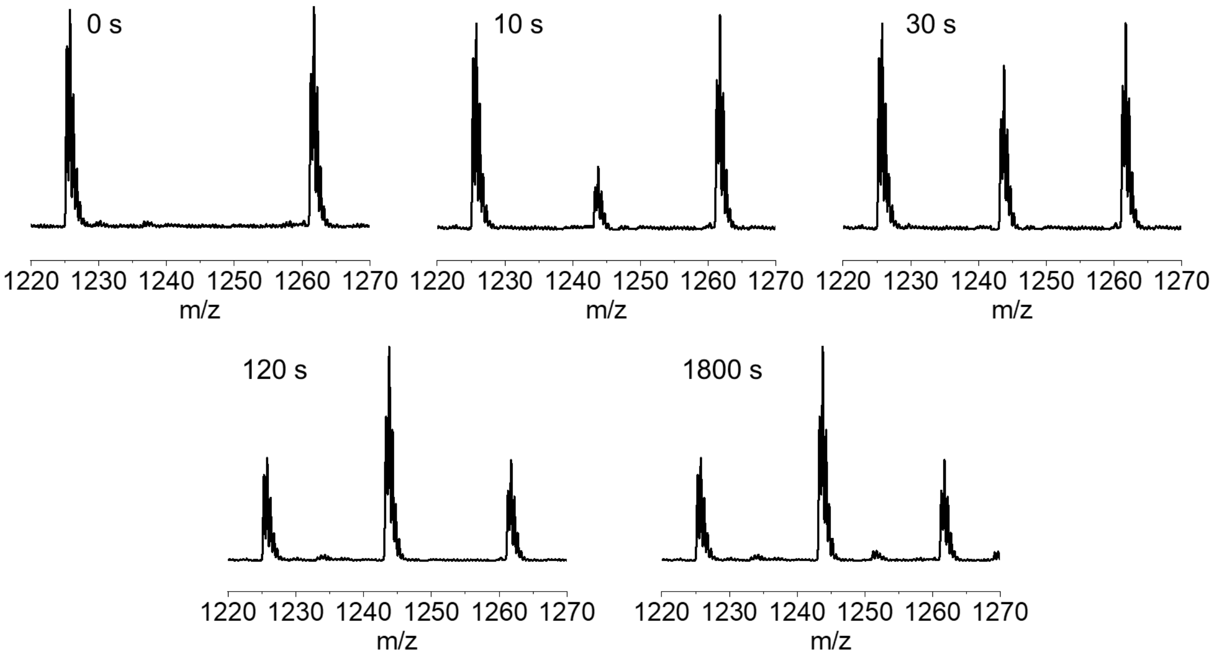

Figure S38 Time dependent ESI-MS spectra of ion exchange for $[La_2L_4]^{2-}$/$[Lu_2L_4]^{2-}$.

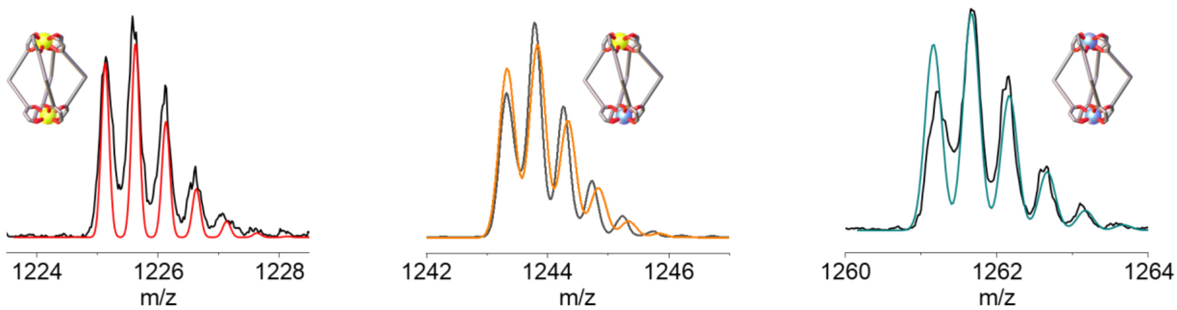

Figure S39 Experimental data black line, simulated patterns for $[La_2L_4]^{2-}$ red line, for $[LaLuL_4]^{2-}$ orange line and for $[Lu_2L_4]^{2-}$ green line after 30 minutes.

Table S10 Relative amounts for $[La_2L_4]^{2-}$/$[Lu_2L_4]^{2-}$ ion exchange derived from ESI-MS.

Time (s)	%$[La_2L_4]^{2-}$	%$[LaLuL_4]^{2-}$	%$[Lu_2L_4]^{2-}$
0*	50.2	0.0	49.8
10	43.2	12.7	44.1
30	30.4	39.8	29.8
120	24.5	50.4	25.1
1800	24.8	50.1	25.1

* Measured mixing the solutions at -18 °C

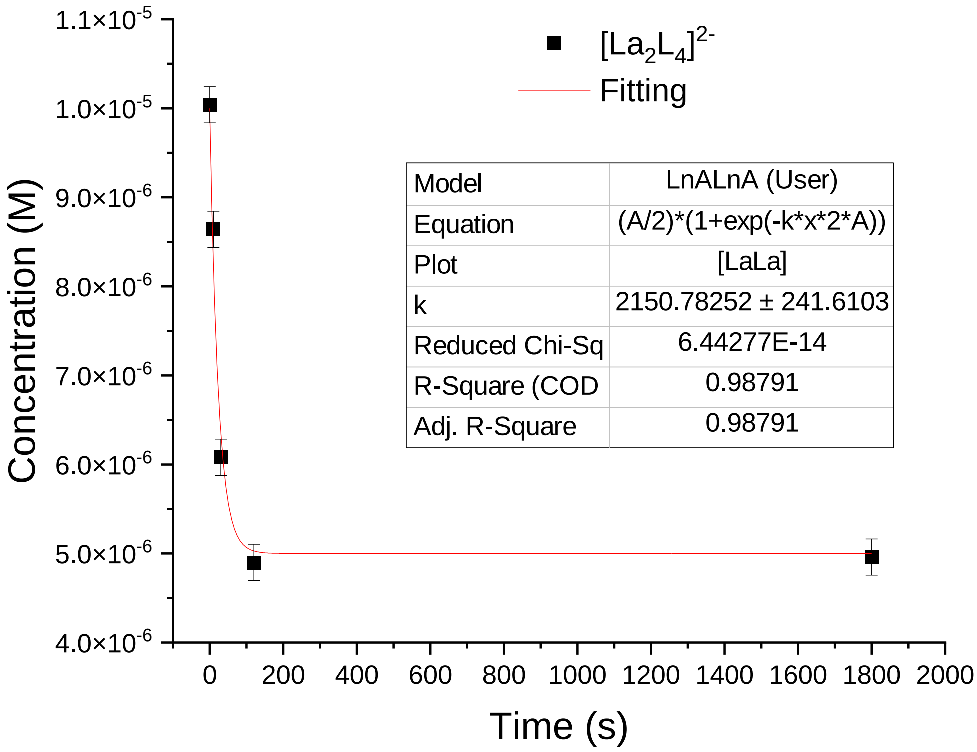

Figure S40 $[La_2L_4]^{2-}$ concentration over time during the $[La_2L_4]^{2-}$/$[Lu_2L_4]^{2-}$ ion exchange derived from ESI-MS.

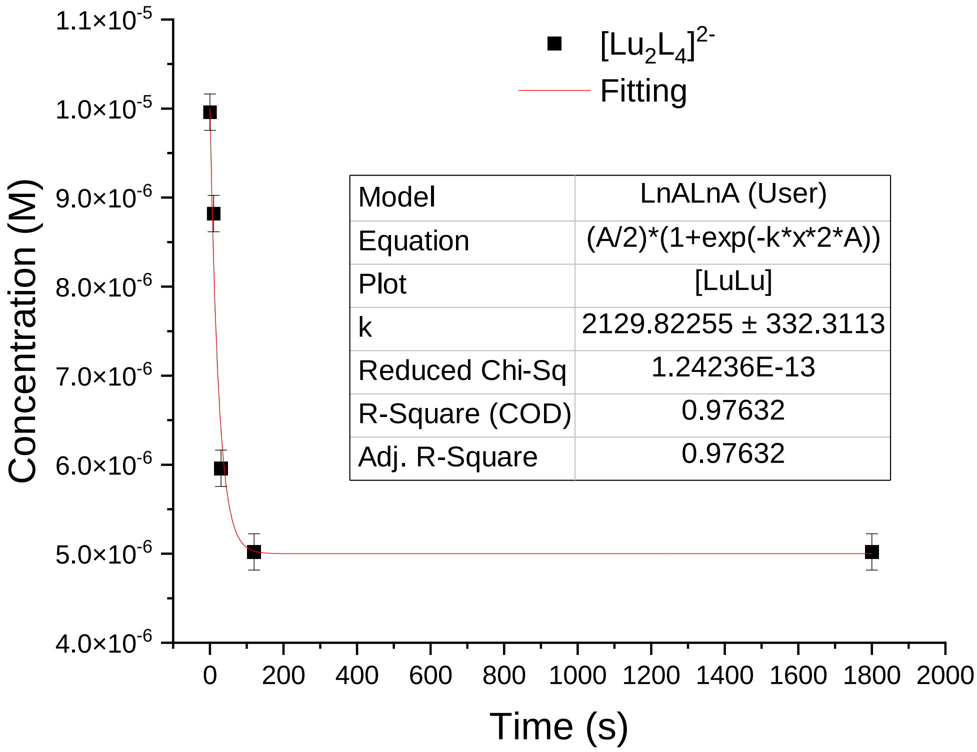

Figure S41 $[Lu_2L_4]^{2-}$ concentration over time during the $[La_2L_4]^{2-}/[Lu_2L_4]^{2-}$ ion exchange derived from ESI-MS.

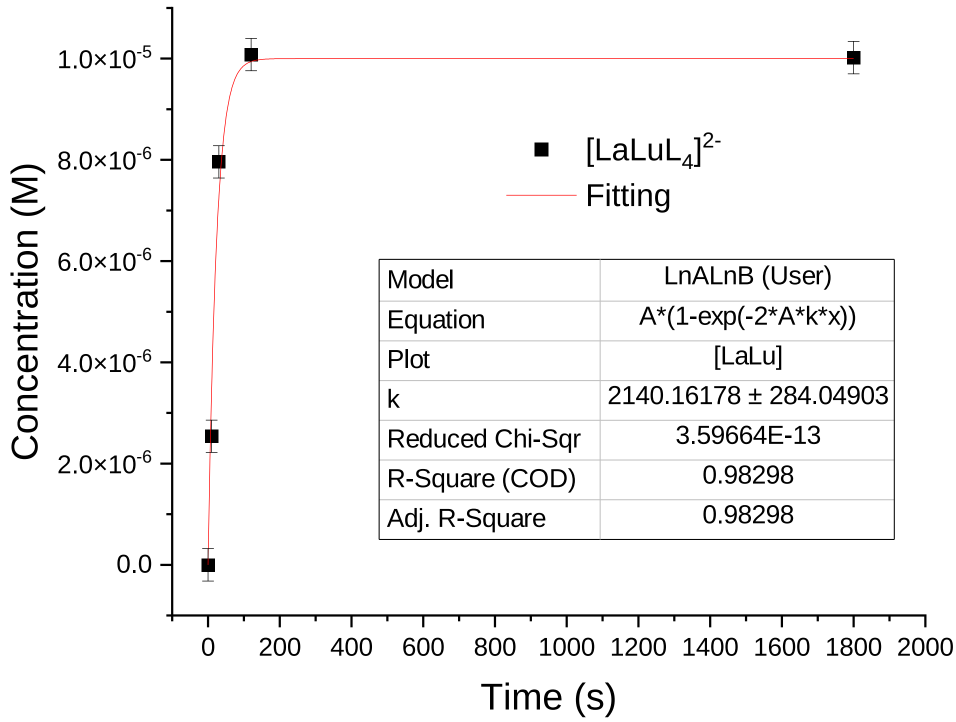

Figure S42 $[LaLuL_4]^{2-}$ concentration over time during the $[La_2L_4]^{2-}/[Lu_2L_4]^{2-}$ ion exchange derived from ESI-MS.

7.7 Ln ion exchange kinetics exponential trend related to ΔEIR

Table S11 k_f, k_b and t_{eq} for the Ln ion exchange.

	$[Tm_2L_4]^{2-}$ + $[Lu_2L_4]^{2-}$ ⇌ 2$[TmLuL_4]^{2-}$ ΔEIR =0.02 Å			
	$[Tm_2L_4]^{2-}$	$[Lu_2L_4]^{2-}$	$[TmLuL_4]^{2-}$	**average**
k_f ($M^{-1}s^{-1}$)	3.22 ± 0.13	3.19 ± 0.02	3.2 ± 0.01	**3.20 ± 0.01**
k_b ($M^{-1}s^{-1}$)	0.81 ± 0.01	0.80 ± 0.01	0.80 ± 0.01	**0.8 ± 0.01**
t_{eq} (min)	1193.1 ± 11.1	1204.3 ± 7.6	1200.5 ± 3.8	**1199.3 ± 4.7**
	$[Eu_2L_4]^{2-}$ + $[Tb_2L_4]^{2-}$ ⇌ 2$[EuTbL_4]^{2-}$ ΔEIR =0.03 Å			
	$[Eu_2L_4]^{2-}$	$[Tb_2L_4]^{2-}$	$[EuTbL_4]^{2-}$	**average**
k_f ($M^{-1}s^{-1}$)	5.26 ± 0.11	5.73 ± 0.15	5.49 ± 0.12	**5.49 ± 0.07**
k_b ($M^{-1}s^{-1}$)	1.32 ± 0.03	1.43 ± 0.04	1.37 ± 0.03	**1.37 ± 0.02**
t_{eq} (min)	730.4 ± 15.3	670.4 ± 17.6	699.8 ± 15.3	**700.2 ± 9.3**
	$[Eu_2L_4]^{2-}$ + $[Tm_2L_4]^{2-}$ ⇌ 2$[EuTmL_4]^{2-}$ ΔEIR =0.08 Å			
	$[Eu_2L_4]^{2-}$	$[Tm_2L_4]^{2-}$	$[EuTm_2L_4]^{2-}$	**Average**
k_f ($M^{-1}s^{-1}$)	12.28 ± 0.68	13.19 ± 0.89	12.86 ± 0.82	**12.78 ± 0.46**
k_b ($M^{-1}s^{-1}$)	3.07 ± 0.17	3.30 ± 0.22	3.22 ± 0.21	**3.2 ± 0.11**
t_{eq} (min)	312.8 ± 17.3	291.3 ± 19.7	298.7 ± 19.0	**300.9 ± 10.8**
	$[La_2L_4]^{2-}$ + $[Eu_2L_4]^{2-}$ ⇌ 2$[LaEuL_4]^{2-}$ ΔEIR =0.11 Å			
	$[La_2L_4]^{2-}$	$[Eu_2L_4]^{2-}$	$[LaEuL_4]^{2-}$	**average**
k_f ($M^{-1}s^{-1}$)	30.17 ± 1.83	29.88 ± 1.70	29.88 ± 1.76	**30.09 ± 1.02**
k_b ($M^{-1}s^{-1}$)	7.54 ± 0.46	7.47 ± 0.44	7.56 ± 0.44	**7.52 ± 0.25**
t_{eq} (min)	127.3 ± 7.7	128.6 ± 7.3	127.1 ± 7.4	**127.7 ± 4.3**
	$[Nd_2L_4]^{2-}$ + $[Er_2L_4]^{2-}$ ⇌ 2$[NdErL_4]^{2-}$ ΔEIR =0.12 Å			
	$[Nd_2L_4]^{2-}$	$[Er_2L_4]^{2-}$	$[NdErL_4]^{2-}$	**average**
k_f ($M^{-1}s^{-1}$)	42.15 ± 2.44	43.10 ± 2.30	43.06 ± 2.80	**42.77 ± 1.46**
k_b ($M^{-1}s^{-1}$)	10.54 ± 0.61	10.78 ± 0.58	10.77 ± 0.70	**10.69 ± 0.36**
t_{eq} (min)	91.2 ± 5.3	89.1 ± 4.8	89.2 ± 5.8	**89.8 ± 3.1**
	$[La_2L_4]^{2-}$ + $[Lu_2L_4]^{2-}$ ⇌ 2$[LaLuL_4]^{2-}$ ΔEIR =0.21 Å			
	$[La_2L_4]^{2-}$	$[lu_2L_4]^{2-}$	$[LaLuL_4]^{2-}$	**average**
k_f ($M^{-1}s^{-1}$)	2150.78 ± 241.61	2130.00 ± 332.31	2140.16 ± 284.05	**2140.31 ± 166.50**
k_b ($M^{-1}s^{-1}$)	537.70 ± 60.40	532.5 ± 83.09	535.04 ± 71.01	**535.08 ± 41.63**
t_{eq} (min)	1.8 ± 0.2	1.8 ± 0.3	1.8 ± 0.2	**1.8 ± 0.1**

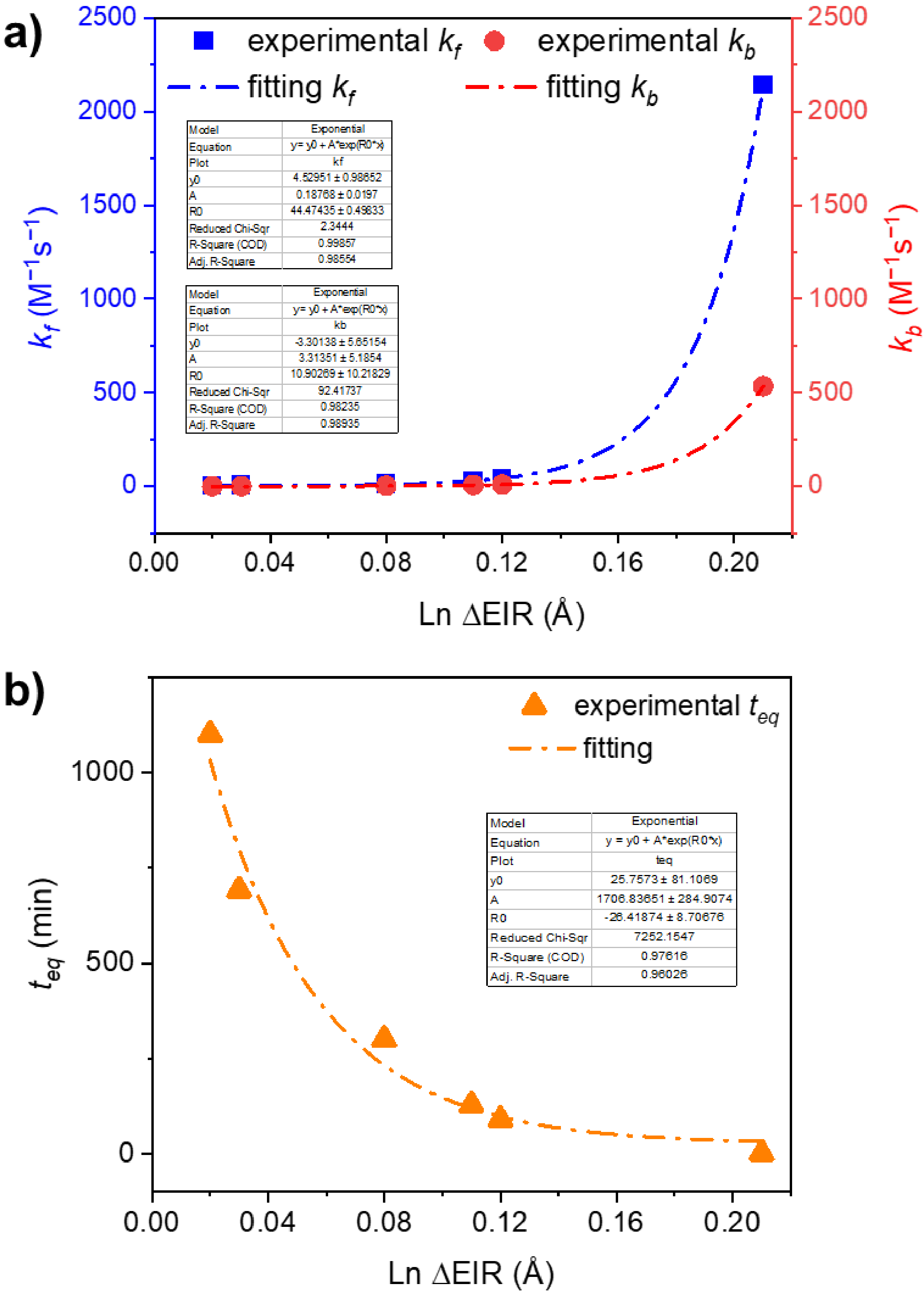

Figure S43 Exponential trends with fitting details of k_f and k_b, and b) of t_{eq} for the Ln ion exchange kinetics depending on Ln ΔEIR.

8. References

1. Dolomanov, O. V., Bourhis, L.J., Gildea, R.J., Howard, J.A.K., and Puschmann, H. (2009). OLEX2: A complete structure solution, refinement and analysis program. J. Appl. Crystallogr. *42*, 339–341. 10.1107/S0021889808042726.
2. Sheldrick, G.M. (2015). SHELXT - Integrated space-group and crystal-structure determination. Acta Crystallogr. Sect. A Found. Crystallogr. *71*, 3–8. 10.1107/S2053273314026370.
3. Sheldrick, G.M. (2015). Crystal structure refinement with SHELXL. Acta Crystallogr. Sect. C Struct. Chem. *71*, 3–8. 10.1107/S2053229614024218.
4. te Velde, G., Bickelhaupt, F.M., Baerends, E.J., Fonseca Guerra, C., van Gisbergen, S.J.A., Snijders, J.G., and Ziegler, T. (2001). Chemistry with ADF. J. Comput. Chem. *22*, 931–967. 10.1002/JCC.1056.
5. Perdew, J.P., and Wang, Y. (1992). Accurate and simple analytic representation of the electron-gas correlation energy. Phys. Rev. B *45*, 13244–13249. 10.1103/PhysRevB.45.13244.
6. Van Lenthe, E., Baerends, E.J., and Snijders, J.G. (1994). Relativistic total energy using regular approximations. J. Chem. Phys. *101*, 9783–9792. 10.1063/1.467943.
7. Van Lenthe, E. (1999). Geometry optimizations in the zero order regular approximation for relativistic effects. J. Chem. Phys. *110*, 8943–8953. 10.1063/1.478813.
8. Lenthe, E. van, Baerends, E.J., and Snijders, J.G. (1993). Relativistic regular two-component Hamiltonians. J. Chem. Phys. *99*, 4597–4610. 10.1063/1.466059.
9. Pye, C.C., Ziegler, T., Lenthe, E. Van, and Louwen, J.N. (2009). An implementation of the conductor-like screening model of solvation within the amsterdam density functional package - Part II. COSMO for real solvents. Can. J. Chem. *87*, 790–797. 10.1139/V09-008.
10. Grimme, S., Ehrlich, S., and Goerigk, L. (2011). Effect of the damping function in dispersion corrected density functional theory. J. Comput. Chem. *32*, 1456–1465. 10.1002/JCC.21759.
11. Sato, S., Ishido, Y., and Fujita, M. (2009). Remarkable Stabilization of M 12 L 24 Spherical Frameworks through the Cooperation of 48 Pd(II)−Pyridine Interactions. J. Am. Chem. Soc. *131*, 6064–6065. 10.1021/ja900676f.
12. Zheng, Y.-R., and Stang, P.J. (2009). Direct and Quantitative Characterization of Dynamic Ligand Exchange between Coordination-Driven Self-Assembled Supramolecular Polygons. J. Am. Chem. Soc. *131*, 3487–3489. 10.1021/ja809788x.
13. Wang, L., Song, B., Khalife, S., Li, Y., Ming, L.-J., Bai, S., Xu, Y., Yu, H., Wang, M., Wang, H., et al. (2020). Introducing Seven Transition Metal Ions into Terpyridine-Based Supramolecules: Self-Assembly and Dynamic Ligand Exchange Study. J. Am. Chem. Soc *142*, 1811–1821. 10.1021/jacs.9b09497.
14. Laidler, K.J. (1987). Chemical Kinetics (Harper & Row).